


Revealing the Physical Conditions around Sgr A* using Bayesian Inference - I. Observations and Radiative Transfer

TOMAS A. JAMES ¹, SERENA VITI ^{2,1}, FARHAD YUSEF-ZADEH,³ MARC ROYSTER,³ AND MARK WARDLE ⁴

¹*Department of Physics and Astronomy, University College London, Gower Street, London WC1E 6BT, UK*

²*Leiden Observatory, Leiden University, PO Box 9513, NL-2300RA, Leiden, The Netherlands*

³*Department of Physics and Astronomy and CIERA, Northwestern University, Evanston, IL 60208, USA*

⁴*Department of Physics and Astronomy and Research Centre for Astronomy, Astrophysics and Astrophotonics, Macquarie University, Sydney, NSW 2109, Australia*

ABSTRACT

We report sub-arcsecond ALMA observations between 272 - 375 GHz towards Sgr A*'s Circumnuclear disk (CND). Our data comprises 8 individual pointings, with significant SiO ($8_7 - 7_6$) and SO ($7 - 6$) emission detected towards 98 positions within these pointings. Additionally, we identify H₂CS ($9_{1,9} - 8_{1,8}$), OCS ($25 - 24$) and CH₃OH ($2_{1,1} - 2_{0,2}$) towards a smaller subset of positions. By using the observed peak line flux density together with a Bayesian Inference technique informed by radiative transfer models, we systematically recover the physical gas conditions towards each of these positions. We estimate that the bulk of the surveyed gas has temperature $T_{\text{kin}} < 500$ K and density $n_{\text{H}} \lesssim 10^6 \text{ cm}^{-3}$, consistent with previous studies of similar positions as traced by HCN clumps. However, we identify an uncharacteristically hot ($T_{\text{kin}} \approx 600$ K) and dense ($n_{\text{H}} \approx 10^6 \text{ cm}^{-3}$) source in the Northeastern Arm. This position is found to be approximately consistent with a gravitationally bound region dominated by turbulence. We also identify a nearby cold ($T_{\text{kin}} \approx 60$ K) and extremely dense ($n_{\text{H}} \approx 10^7 \text{ cm}^{-3}$) position that is again potentially bound and dominated by turbulence. We also determine that the total gas mass contained within the CND is $M_{\text{CND}} \approx 4 \times 10^4 M_{\odot}$. Furthermore, we qualitatively note that the observed chemical enrichment across large scales within the CND is consistent with bulk grain processing, though multiple desorption mechanisms are plausibly responsible. Further chemical modelling is required to identify the physical origin of the grain-processing, as well as the localised H₂CS and OCS emission.

Keywords: astrochemistry, galaxies: ISM, ISM: clouds, ISM: kinematics and dynamics, methods: observational, methods: statistical

1. INTRODUCTION

The Galactic Center, and within it the Central Molecular Zone, has long been identified as a uniquely extreme environment within the Milky Way owing to the $(4.154 \pm 0.014) \times 10^6 M_{\odot}$ supermassive black hole known as Sgr A* that resides there (Gillessen et al. 2009; Abuter et al. 2019). Such an environment has important consequences for theories of galactic evolution and dynamics, as the Galactic Center can be used as a high-resolution laboratory for studying the nuclei of external galaxies. However, it also has a profound impact on the

ories of both ISM physics and chemistry under extreme conditions, especially when considering dense molecular gas as precursors to star formation.

Morphologically, the inner few pc of the Galactic Center is chaotic and multifaceted. Centrally, Sgr A* is situated within a trifecta of ionised gas streams known as the Galactic Center Mini Spiral, or GCMS (Lacy et al. 1980; Ekers et al. 1983). Surrounding the GCMS is an extensive torus or ring like structure of turbulent molecular gas known as the Circumnuclear ring or Circumnuclear disk, herein referred to as the CND (e.g. Christopher et al. 2005). The diffuse region between Sgr A* and the CND - known as the Central Cavity - is home to a collection of young and evolved stellar objects, including ≈ 100 OB stars (Eckart et al. 2004; Paumard et al. 2006;

Lu et al. 2008; Mauerhan et al. 2010) that are thought to considerably increase the photoionisation rate within and around Sgr A* (Genzel et al. 1996; Paumard et al. 2006).

Studies of the CNM are complicated by a degree of uncertainty surrounding its exact morphology and kinematics. The extent of the CNM is easily identified in low J -transitions of molecules such as CS, H₂CO and SiO (Martin et al. 2012; Tsuboi et al. 2018) as well as dust continuum emission (Lau et al. 2013) and high J -transitions of molecules like ¹²CO (Goto et al. 2013). Such observations identify the CNM as extending radially from ~ 1.6 pc outwards to ~ 5 – 7 pc from Sgr A* (Smith & Mac Low 2014), rotating at ~ 110 km s⁻¹ between 2–5 pc (Ghez et al. 2005; Genzel et al. 2010).

However, the CNM is not continuous or indeed uniform as occasional regions devoid of emission known as ‘gaps’ are observed, in turn indicating that different molecules are mapping different regions of the CNM. Notable amongst these gaps is that seen in HCN (1-0) towards the North of Sgr A*. Wright et al. (2001) propose that this gap is caused by an infalling arm of the Galactic Center Mini Spiral pushing through the CNM as it falls towards Sgr A* proper, producing OH maser emission (Yusef-Zadeh et al. 1999) in the process. It is therefore clear that the gas conditions within the CNM are highly non-uniform and position dependent.

In addition, the interior of the CNM is highly irregular and inhomogeneous, exhibiting clump like structures of size 0.14 – 0.43 pc distributed throughout when viewed in the near-IR HCN (1-0) transition (Guesten et al. 1987; Jackson et al. 1993; Christopher et al. 2005). A number of theories regarding the physical conditions within these clumps exist, and Genzel et al. (2010) extensively summarises the two prevailing theories as the ‘transient’ and ‘virial’ scenarios. In summary, the transient scenario suggests that the clumps are typically warm (> 100 K), less dense ($< 10^6$ cm⁻³) and tidally unstable with transient lifetimes $\approx 10^5$ yrs. Conversely, the virial scenario states that these clumps are cooler (< 100 K), dense (10^7 – 10^8 cm⁻³) and tidally stable with lifetimes $> 10^7$ yrs. Crucially, this stability affords these clumps the opportunity to begin in-situ star formation. The tidal instability, and therefore shorter lifetime estimate in the transient scenario, would not permit any gravitationally bound object formation.

Within the detected clumps, Tsuboi et al. (2018) estimate that some of the relatively low density regions have gas densities in the range $0.9 - 6 \times 10^4$ cm⁻³. Smith & Wardle (2014) estimate denser HCN bright cores to have densities in the range $0.1 - 2 \times 10^6$ cm⁻³. Smith & Wardle (2014), and independently Mills et al. (2013), find that

the HCN clumps have conditions consistent with that outlined in the transient scenario. Crucially, such studies have not explored kinetic gas temperatures > 250 K and thus could fail to highlight hot and dense embedded sources. However, Smith & Wardle (2014) theorise that the CNM is subject to such large tidal shear that local star formation is unlikely to occur within the CNM in the absence of some triggering event. This tidal shear condition could be overcome should self-gravity dominate according to $\sim 10^7(r/\text{pc})^{-3}$ cm⁻³ (Yusef-Zadeh et al. 2017). Assuming that the bulk of the CNM is found between 1.5 – 2 pc from Sgr A* as traced by HCN (Christopher et al. 2005), then exceeding the tidal shear condition would require gas density between $\approx 2 \times 10^6$ cm⁻³ at $r \approx 1.5$ pc, dropping to $\approx 2 \times 10^5$ cm⁻³ at $r \approx 2$ pc. Satisfying this criterion is essential for in-situ star formation to occur within these clumps.

C-type shocks originating from clump-clump collisions have been proposed as an efficient heating mechanism within the CNM owing to the high observed temperatures of $T_{\text{kin}} > 200$ K (Bradford et al. 2005; Harada et al. 2015). However, star formation as a process also presents multiple opportunities to drive C-type shocks in to the surrounding gas, in turn chemically enriching the surrounding ISM in a similar manner to clump-clump collisions. SiO and SO - as well as other S-bearing species such as H₂S - are all known shock tracers (Martin-Pintado et al. 1992; des Forêts et al. 1993) as a result of shock-driven evaporation of grain surface and/or mantle. Subsequent reaction of the evaporated species in the gas-phase, for example Si and S with O, can produce molecules such as SiO and SO. Previous simulations (Martin-Pintado et al. 1992; Flower et al. 2003; Holdship et al. 2017; James et al. 2020) have used these molecules to great effect when tracing star formation related shocks under standard interstellar conditions. However, as already demonstrated the CNM and its surroundings represent extreme departures from standard interstellar conditions. For example, the OB star population in the Central Cavity could increase the photoionisation rate substantially. In addition to this, the cosmic-ray ionisation rate within the Central Molecular Zone is much larger than in other regions of the galaxy. Both Yusef-Zadeh et al. (2007) and Goto et al. (2013) estimate this could extend to an upper limit of between $10 - 10^4 \zeta$ s⁻¹ assuming a standard galactic ionisation rate of $\zeta \approx 3 \times 10^{-17}$ s⁻¹.

Additionally, the Central Molecular Zone and its immediate surroundings are known to exhibit large scale distributions of molecules such as CH₃OH (Gottlieb et al. 1979) as well as HCN, HNC and HCO⁺ emission (Jones et al. 2011). Detection of these molecules,

specifically CH₃OH, in abundance is again typical of regions that have undergone grain processing. As noted by Turner (1998), the gas-phase formation routes and efficiencies of CH₃OH in particular cannot account for its measured abundance within the ISM. Instead, Turner (1998) found that CH₃OH forms readily via successive Hydrogenation of CO on the grain surface. Subsequent desorption - UV photodesorption being the dominant mechanism in translucent clouds - then releases CH₃OH in to the gas-phase (Turner 1998). Crucially, these formation and desorption pathways are consistent with measured gas-phase abundances of CH₃OH. Yusef-Zadeh et al. (2013) also investigated this phenomenon by comparing chemical models to CH₃OH observations to constrain the mechanism responsible for its gas-phase existence. As Molinari et al. (2011) highlight, the dust temperature $T_{\text{dust}} \leq 40$ K within the Central Molecular Zone is too low for thermal desorption to be significant. They therefore conclude that cosmic-ray desorption represents the dominant desorption mechanism of CH₃OH within the Central Molecular Zone. However, on smaller scales applied to the CND both Latvakoski et al. (1999) and Lau et al. (2013) find that the dust temperature can vary positionally from 40 K – 200 K, in turn showing that thermal desorption could become significant in sub-regions of the CND where the dust temperature exceeds ≈ 100 K. Consequently, detections of molecules such as SiO, SO and CH₃OH are direct tracers of underlying physical events such as shocks, and/or regions that have undergone grain processing.

Broadly, the detected emission intensity of these molecules is a function of the region’s physical gas conditions which are, in turn, a function of the physical processes occurring within the gas. One may derive estimates of the kinetic gas temperature T_{kin} , Hydrogen number density n_{H} and molecular column densities N_{spec} using radiative transfer codes such as RADEX (Van Der Tak et al. 2007) in order to understand these processes in more detail. Crucially, repeating this procedure for each position within and throughout a sample of beam pointings allows mapping of the gas conditions across those pointings, permitting a larger scale understanding of the physics and chemistry driving an object’s evolution.

Within this paper we present $0.38'' \times 0.31''$ spectral observations of Sgr A*’s Circumnuclear Disk, and apply the aforementioned radiative transfer methodology to this data. We present these observations in Section 2 before discussing their implications in Section 3. In Section 4 we outline our statistical process coupled to radiative transfer that infers the physical gas conditions towards each position. Sections 5 and 6 presents the

Table 1. Details of the observational pointings used to collect data for this study. Shown are the Field ID for each pointing, alongside its central RA and Dec and the associated sensitivity. To assist future reference, Field IDs are prepended to numerical positions where molecular emission is identified, e.g. N1, N2 etc. Each pointing has size $\sim 21''$ at 300 GHz. Spatial coverage for each pointing is shown in Figure 1.

Field ID	Pointing Center α, δ (J2000)	Sensitivity (mJy beam ⁻¹ chan ⁻¹)
N	17 ^h 45 ^m 40.60 ^s , -29°00′20.00″	4.98
G	17 ^h 45 ^m 43.80 ^s , -29°00′20.00″	5.24
D	17 ^h 45 ^m 41.75 ^s , -28°59′47.69″	5.34
H	17 ^h 45 ^m 39.49 ^s , -28°59′51.02″	5.02
J	17 ^h 45 ^m 38.00 ^s , -29°00′01.00″	5.24
K	17 ^h 45 ^m 38.30 ^s , -29°00′40.00″	5.35
L	17 ^h 45 ^m 39.95 ^s , -29°01′03.50″	5.46
M	17 ^h 45 ^m 41.32 ^s , -29°01′01.63″	5.39

results of our modelling for each considered parameter, before Section 7 discusses the possible emission mechanisms responsible for the observed complexity as well as our mass estimates.

2. OBSERVATIONS

ALMA Cycle 2 Band 7 (272 - 375 GHz) observations (Project Code 2013.1.01242.S) that target various SiO transitions towards the CND are utilized for this investigation. The data presented in Figure 1 and Table 1 was obtained on 2015 June 8 and consists of 8 pointings with the 12m array. Each pointing has a total field of view of $19.608''$ and a synthesized beam of $0.38'' \times 0.31''$ with PA = -72° corresponding to an on sky spatial scale of approximately 0.014×0.012 pc. We thus assume a beam filling factor of unity. The total integration time for each source is 151 s with the relevant baseline tuned at the rest frequency of SiO (7 - 6) (303.926809 GHz) along with a total bandwidth of 937.5 MHz corresponding to ~ 900 km s⁻¹. The raw data product has a velocity resolution of ~ 0.5 km s⁻¹ (3840 channels).

The data was calibrated with the assistance of standard observatory scripts using CASA 4.7.0 (McMullin et al. 2007). CASA was also used to image the data with a $0.05''$ pixel size and 2 km s⁻¹ (2.03 Hz) channel width. A Brigg’s robustness parameter of 0.5 was utilized. The result achieved a sensitivity of ~ 5 mJy, as shown in Table 1. Integrated and peak intensity maps were used to visually identify molecular line emission in

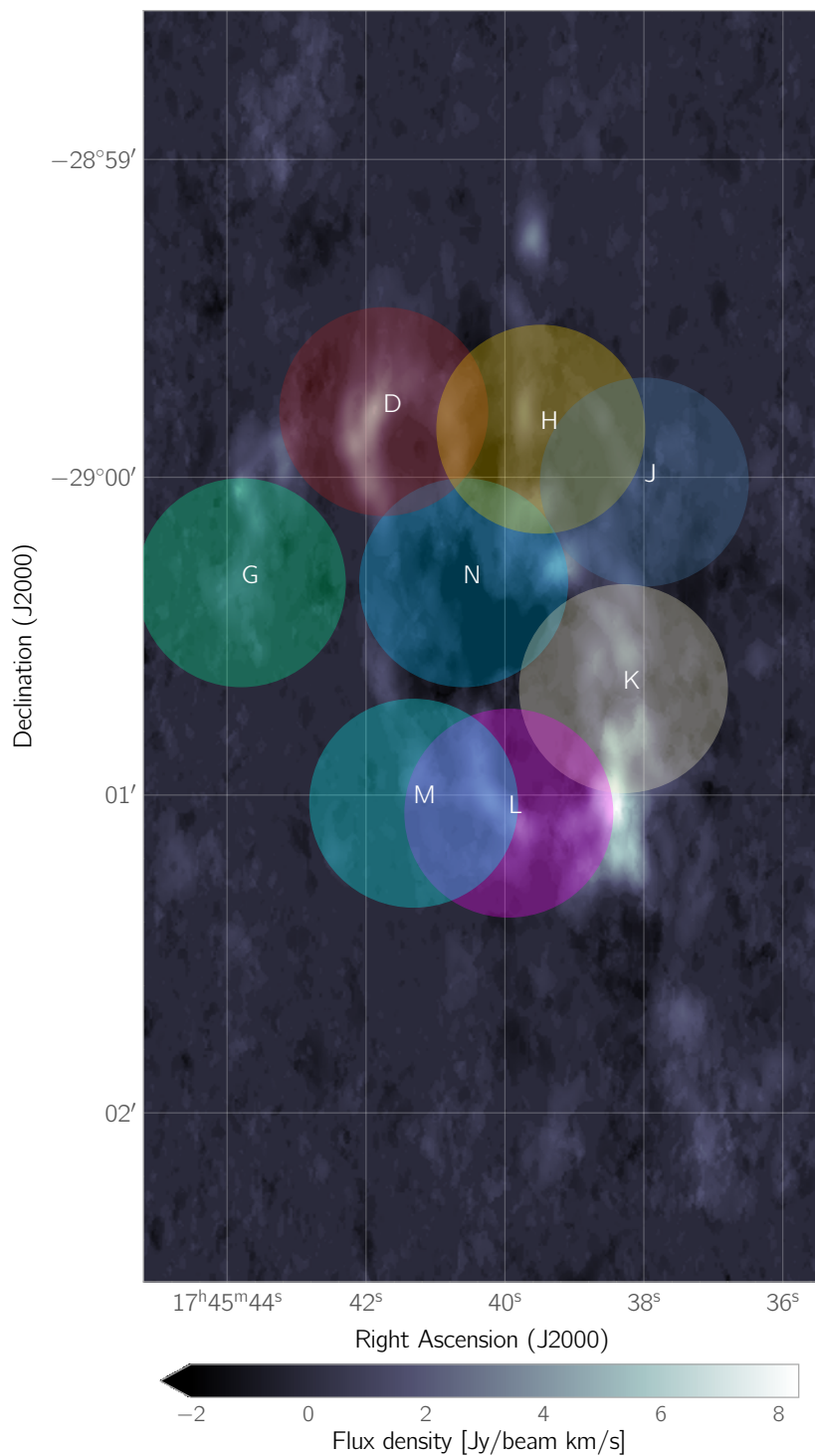


Figure 1. The 8 ALMA pointings of size 21'' at 300 GHz that comprise our data, overplotted on an HCN emission map of Sgr A* and its surrounding Circumnuclear disk (CND). Details of the individual pointings can be found in Table 1. We follow the naming convention in [Christopher et al. \(2005\)](#), as well as Figure 2 of [Montero-Castaño et al. \(2009\)](#), for referring to regions within and around the CND, e.g. pointing G targets the Northeastern Arm whilst pointings M and L target the Southern Extension. Note: the G pointing is distinct and separate from the dust enshrouded sources of G1 and G2 in [Ciurlo et al. \(2020\)](#).

the data cubes, and these identified lines are listed in Table 3 within Appendix B.

2.1. *CND spectra*

Spatial representations of the 8 pointings that comprise our observations are shown in Figure 1. The spectra for each of the 99 positions is shown in Appendix A, whilst the spectra derived quantities are shown in Table 3 of Appendix B. The circular regions shown in Figure 1 represent the approximate field of view of each pointing corresponding to $21''$ at 300 GHz. Within this, we follow the naming convention adopted in Christopher et al. (2005) as well as Montero-Castaño et al. (2009) for surveying regions of the CND. As such, the G pointing surveys the Northeastern Arm of Sgr A*, whilst all other pointings survey the interior of the CND. We note that the G-pointing and its sources within are distinct and separate from the dust enshrouded sources G1 and G2 highlighted by Ciurlo et al. (2020). Within these pointings, each position contains at least either an SiO ($7-6$) or SO (8_7-7_6) line. Only 2 observations - N3, IRS7 - contain only SiO ($7-6$) and SO (8_7-7_6) respectively. 96 observations within the data contain both SiO ($7-6$) and SO (8_7-7_6) transitions; the exception is the M4 source in which we do not detect SiO ($7-6$) but do detect both SO (8_7-7_6) and CH₃OH ($2_{1,1}-1_{0,2}$) transitions.

Whilst SiO and SO are the most commonly detected molecules, CH₃OH forms the third most commonly detected species, being present towards 16 different positions. CH₃OH ($2_{1,1}-1_{0,2}$) is not detected in any L pointing. In fact, it is most commonly observed within the N pointing. Additionally, our detections of H₂CS ($9_{1,9}-8_{1,8}$) are only found within a small grouping of observations within the G pointing. Furthermore, we find OCS ($25-24$) to have even further localisation, being present in only two sources: G2 and K13a. Curiously, G2 and K13a are located in two opposite, distinct regions within the CND and do not appear to be causally or spatially related to one another.

3. QUALITATIVE GAS CHARACTERISTICS

Given the commonality of SiO and SO emission, the ratio $I_{\text{SiO}}/I_{\text{SO}}$ is a useful diagnostic of the most intense emission regions. Figure 2 shows this ratio as a function of each position's location and extent. Each aperture within this plot represents the on-sky location of a detection described in Section 2, with the size of the aperture being approximately equivalent to the total extent in beams as given in Appendix B. The colour scale employed to fill these apertures is representative of the $I_{\text{SiO}}/I_{\text{SO}}$ ratio as indicated by the vertical colour bar.

The underlying image represents HCN emission of the CND. It's flux density is defined according to the horizontal colour bar.

Within Panel 1, the observations G1, G2, G3a and G3b sit along a filament of HCN emission, whilst G4 and G5 are situated outside of this structure. As noted previously, we highlight that these positions and separate and distinct from the G1 and G2 sources identified in Ciurlo et al. (2020). However, the presence of the filament appears to have negligible effect on the $I_{\text{SiO}}/I_{\text{SO}}$ ratio as all sources < 1 . G1 is found to have a low $I_{\text{SiO}}/I_{\text{SO}}$ ratio of ≈ 0.8 , whilst G2 is observed to be slightly lower at ≈ 0.75 . The ratio at G3a is consistent with G1, whilst G3b is found to be slightly lower again at ≈ 0.7 . However, G4 has a ratio approximately consistent with G2, whilst G5 has ratio consistent with that of G1. Nevertheless, the $I_{\text{SiO}}/I_{\text{SO}}$ ratio implies that the gas in this region has marginally greater SO emission than SiO, in turn indicating a higher density of SO than SiO within this region.

When considering Panel 2, it is immediately evident that there is again very little variation in the $I_{\text{SiO}}/I_{\text{SO}}$ ratio across the area covered. With the exception of K15a and K17, every other observation in this inset plot shows $I_{\text{SiO}}/I_{\text{SO}} \lesssim 1$. Interestingly, K12, K13a and K13b sit along a ridge that demarcates a bright HCN emission cloud from its surrounding background. It is this region that is subject to close interaction between the Galactic Center Mini Spiral and the molecular gas within the CND. From the $I_{\text{SiO}}/I_{\text{SO}}$ ratio, it would appear that this ridge shows stronger SO emission than SiO emission.

Panel 3, much like Panel 2, shows very little variation in ratio. The only exception to this uniformity is the multi-component gas at L19 and L30. L19's surrounding gas shows only single component behaviour, making the multi-component nature of L19 puzzling. Unfortunately, L30 does not have any nearby observation to compare with, though it is worth noting that the $I_{\text{SiO}}/I_{\text{SO}}$ ratio for the second component here is the largest ratio seen in the data at ≈ 12 . This stands in stark contrast to the rest of the observations in Panel 3 whose ratios are significantly lower and much more uniform at $\lesssim 1$.

Moreover, in addition to L19 and L30 we find 2 further sources in our observations - D3, and K8b - that exhibit multi-component behaviour. Curiously, each of these sources contains only SiO and SO lines.

Broadly, Figure 2 seemingly indicates that the energetics of the CND do not vary significantly throughout its extent, or from region to region. However, $I_{\text{SiO}}/I_{\text{SO}}$ is inherently degenerate as the ratio when $I_{\text{SO}} \ll 1$ can also be the same as when $I_{\text{SiO}} \gg 1$. We therefore utilise

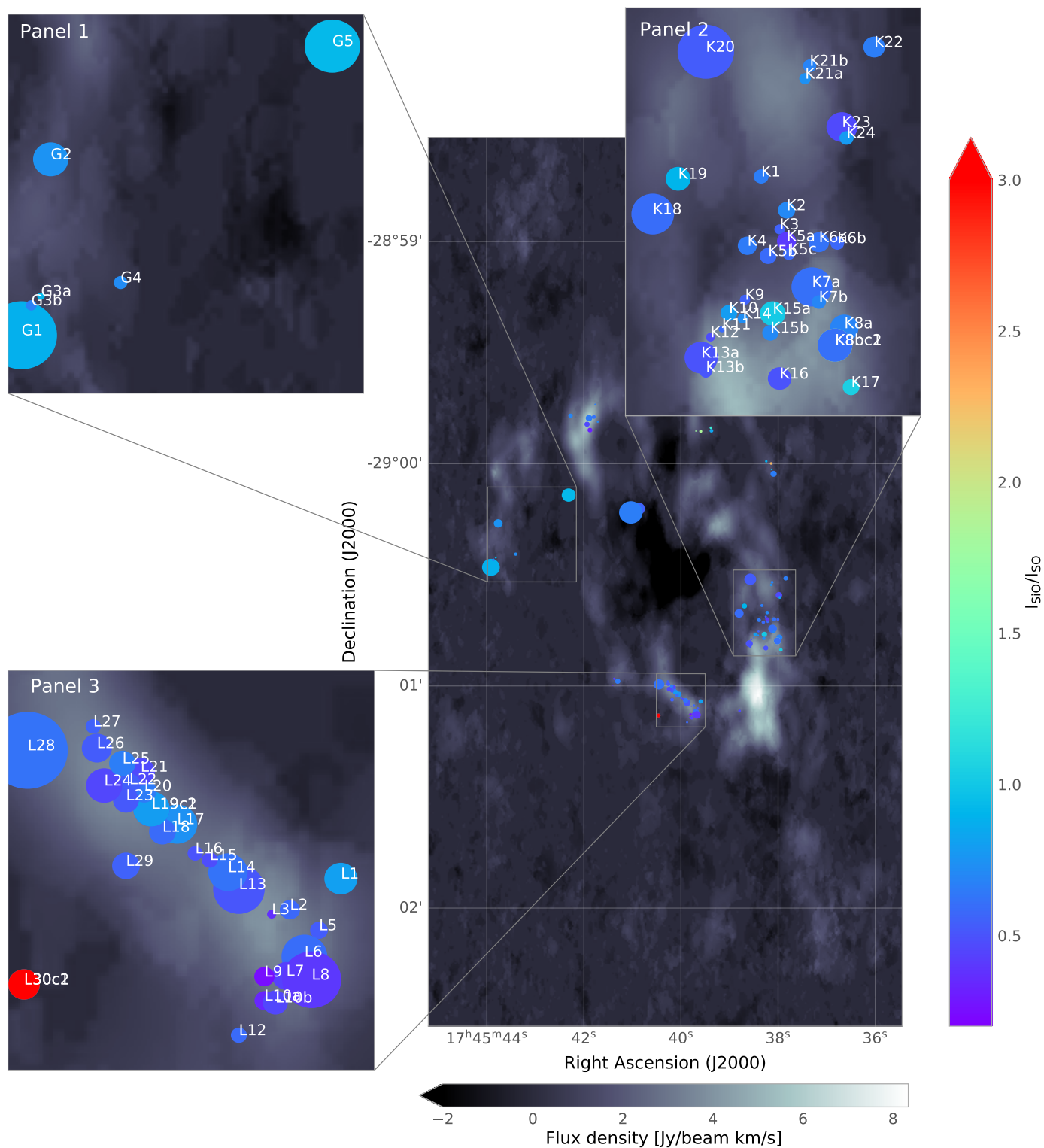


Figure 2. The ratio of observed SiO to SO flux densities $I_{\text{SiO}}/I_{\text{SO}}$ for each position within the 8 pointings where SiO and SO are conclusively identified. Each circle represents the extent of each position in approximate synthesised beam sizes, and its colour denotes the ratio $I_{\text{SiO}}/I_{\text{SO}}$ towards that region as per the vertical colour bar. Inset plots are labelled as Panel 1 – 3 and show groupings of observations and their observational designations. Key here is the uniformity in $I_{\text{SiO}}/I_{\text{SO}}$ throughout the dataset; most positions show $I_{\text{SiO}}/I_{\text{SO}} < 1.5$.

a quantitative approach to deriving the gas conditions within each observation.

4. GAS CONDITION INFERENCE PROCEDURE

Both the physics and chemistry of interstellar gas are entangled and thus form a system that is extremely non-linear and non-trivial to model. We simplify this modelling challenge by approaching the problem with non-LTE radiative transfer in RADEX (Van Der Tak et al. 2007) coupled to a Bayesian inference procedure. Within this scheme we may inform the radiative transfer with a set of independent random variables that define the physical gas conditions. Monte Carlo methods can then be used to explore the physical condition parameter space, in turn converging on the most likely gas conditions for each region. Additionally, this approach minimises the number of variables required to model the CND gas, in turn allowing us to determine the physical gas conditions with a minimal number of assumptions. A key assumption for applying RADEX is, however, that the transitions under consideration are optically thin, as is likely the case.

4.1. Radiative transfer

Using this approach, we utilise the radiative transfer code RADEX (Van Der Tak et al. 2007) to compute the emitted line flux density of the relevant transition for a parcel of gas with physical conditions described by the set of parameters $\mathcal{S} = \{T_{\text{kin}}, n_{\text{H}}, N_{\text{spec}}\}$. T_{kin} is the gas temperature, n_{H} is the molecular Hydrogen gas number density and N_{spec} is the column density of the relevant species under consideration. Owing to the strong UV heating supplied by the OB star population, as well as the high temperatures inferred in the CND from previous observations, we explore temperatures up to 1000 K. We used RADEX owing to its non-LTE molecular excitation capabilities, as well as its widespread use in studies that model interstellar spectra (e.g. Beuther et al. 2008; Lique et al. 2009; Van Dishoeck et al. 2021), including towards the Galactic Center (e.g. Wirström et al. 2010; Amo-Baladrón et al. 2011; Armijos-Abendaño et al. 2020). We intend to apply more detailed chemical modelling to these regions in future in order to further understand their phenomenology. All species within this study utilise temperature dependent collisional data from the LAMDA database (Schöier et al. 2010). For temperatures outside of the calculated temperature range that LAMDA reports, RADEX fixes the collisional rate constant to the rate constant at the nearest temperature. For SiO, the collisional data has been calculated up to and including collisional temperatures of 1000 K. Inspecting the

rate constants for SiO ($8_7 - 7_6$) reveals relatively uniform (within a factor of 2) behaviour across the a-priori temperature range. Considering a similar process for SO ($7 - 6$) we note that the collisional rates have been determined up to 300 K. Much like SiO, the collisional data for SO is similarly constant within the calculated temperature range. We therefore assume that, given the similar chemical compositions and masses of SiO and SO, the same uniformity in collisional rates is evident beyond 300 K. We note similar behaviour within the collisional data for the other molecular transitions detected in our data, and we therefore apply the same assumption to all molecules and transitions detected in our observations.

Additionally, each observation presented in Section 2 has been normalised to units of mJy/beam and thus assumes that each observation fills the beam. This renders RADEX computed flux densities, as RADEX assumes a beam filling factor of 1, directly comparable to the observational flux densities presented. The assumption of a beam filling factor of unity is further justified as the linear scale of our observations is sufficient to guarantee that the only emission within the beam is from the targeted gas. Each source is also fully resolved, in turn ensuring they fill each beam.

Repeating this procedure for each species and each transition in a given observation allows us to construct a model θ that represents the synthetic flux density emitted from a region of gas at temperature T_{kin} and gas density n_{H} comprising species column densities N_{spec} . Constructing the model in this manner assumes that all emission lines contained within it originate from the same thermal component. As Section 2 showed, our observations are consistent with a single component. Where not, it is clear and distinct that 2 components are present, either through distinctly different linewidths or bi-modal line profiles, and they are thus treated as essentially two separate sources, in turn being analysed with 2 distinct models.

However, given the complexity of the underlying physics and chemistry, and indeed their associated degeneracy, it is useful to statistically survey the entire parameter space across each dimension in order to better understand and identify the probable conditions within each observation. An ideal process with which to do this utilises Bayesian Inference.

4.2. Bayesian Inference

Bayesian Inference is a method of using conditional probability to build statistical parameter distributions

for multi-dimensional data. Unsurprisingly, it utilises Bayes’ Theorem, defined in Equation 1.

$$P(\boldsymbol{\theta}|\mathbf{d}) = \frac{P(\mathbf{d}|\boldsymbol{\theta})P(\boldsymbol{\theta})}{P(\mathbf{d})} \quad (1)$$

$P(\boldsymbol{\theta}|\mathbf{d})$ is defined as the probability of the model $\boldsymbol{\theta}$ fitting the data \mathbf{d} given that the data is correct (known as “the posterior probability”). $P(\mathbf{d}|\boldsymbol{\theta})$ is the probability of having obtained the data \mathbf{d} given a particular model $\boldsymbol{\theta}$ (known as “the likelihood”). $P(\boldsymbol{\theta})$ is defined as the probability of the model $\boldsymbol{\theta}$ being correct (“the prior”) and $P(\mathbf{d})$ is the probability that the data is correct (“the evidence”). We define the data as being the observed flux densities, whilst the model is the equivalent line flux density determined from RADEX as defined in Section 4.1.

We assume flat priors in log space such that within each dimension, any value is equally as likely as any other providing that such a value falls within the non-zero prior range. The non-zero ranges used for these priors, and in turn the extent of parameter spaces explored, are shown in Table 2.

Table 2. The pre-constrained parameter spaces surveyed in this preliminary study for each explored dimension. T_{kin} represents the gas kinetic temperature, n_{H} is the Hydrogen gas number density and N_{spec} is the species column density corresponding to the species spec.

Parameter	Range	Unit
T_{kin}	60-1000	K
n_{H}	10^3 - 10^7	cm^{-3}
N_{SiO}	10^{12} - 10^{16}	cm^{-2}
N_{SO}	10^{12} - 10^{16}	cm^{-2}
$N_{\text{CH}_3\text{OH}}$	10^{14} - 10^{17}	cm^{-2}
$N_{\text{H}_2\text{CS}}$	10^{12} - 10^{15}	cm^{-2}
N_{OCS}	10^{12} - 10^{15}	cm^{-2}

We constrain the upper and lower limits of column density for each molecule to explore by estimating the LTE derived column density for the upper and lower limits of temperature shown in Table 2. This makes use of molecular data provided by Splatalogue (Remijan et al. 2007).

We compute the likelihood using the likelihood function defined in Equation 2.

$$P(\mathbf{d}|\boldsymbol{\theta}) = \exp\left(-\frac{1}{2}\sum_i \frac{(d_i - \theta_i)^2}{\sigma_i^2}\right) \quad (2)$$

Where the summation term represents the Chi-squared statistic. Within Equation 2, d_i is the i^{th} value of the data, θ_i is the i^{th} value of the model corresponding to d_i and σ_i is the error associated with d_i .

By implementing this Bayesian procedure we sample from the underlying posterior distribution using randomly sampled variables that define the gas condition. These variables thus form the set \mathcal{S} . To perform this sampling we use the affine-invariant MCMC sampler `emcee` (Foreman-Mackey et al. 2013). `emcee` uses a number of “walkers” to systematically sample the parameter space across a number of steps, in turn constructing a series of Markov Chains. All walkers therefore define a representation of the underlying posterior distribution, allowing us to identify statistically informed estimates of the most likely gas condition towards each observation. We use an ensemble of 500 walkers and we run each walker for a maximum of 1×10^4 steps. Every 100 steps we assess convergence in each dimension using the Gelman-Rubin statistic (Gelman & Rubin 1991). We halt our sampling if convergence is judged to have been achieved across all dimensions. We follow Brooks & Gelman (1998) in judging successful convergence when the Gelman-Rubin diagnostic for each dimension < 1.2 . For additional confidence, we select a cut-off of 1.15 for achieving sample convergence. In addition and where relevant we also visualise our chains using `ChainConsumer` (Hinton 2016).

This approach has a number of distinct advantages when deriving physical gas conditions. Firstly, the number of variables required to define the gas is limited to those required by RADEX, resulting in a relatively low number of dimensions overall. Additionally, within this scheme each dimension is entirely free and is not causally related to any other. As such, we derive the gas conditions with almost no a-priori knowledge of the local chemistry. The affine-invariant nature of the `emcee` sampler thus allows convergence to be achieved independently of the underlying physics and/or chemistry beyond radiative transfer, thus reducing uncertainty and bias.

5. INFERENCE RESULTS: CORNER PLOTS FOR INDIVIDUAL SOURCES

Figure 3 shows an example of the corner plot for the G2 source. G2 contains the largest number of lines in our sample that our detected towards one region.

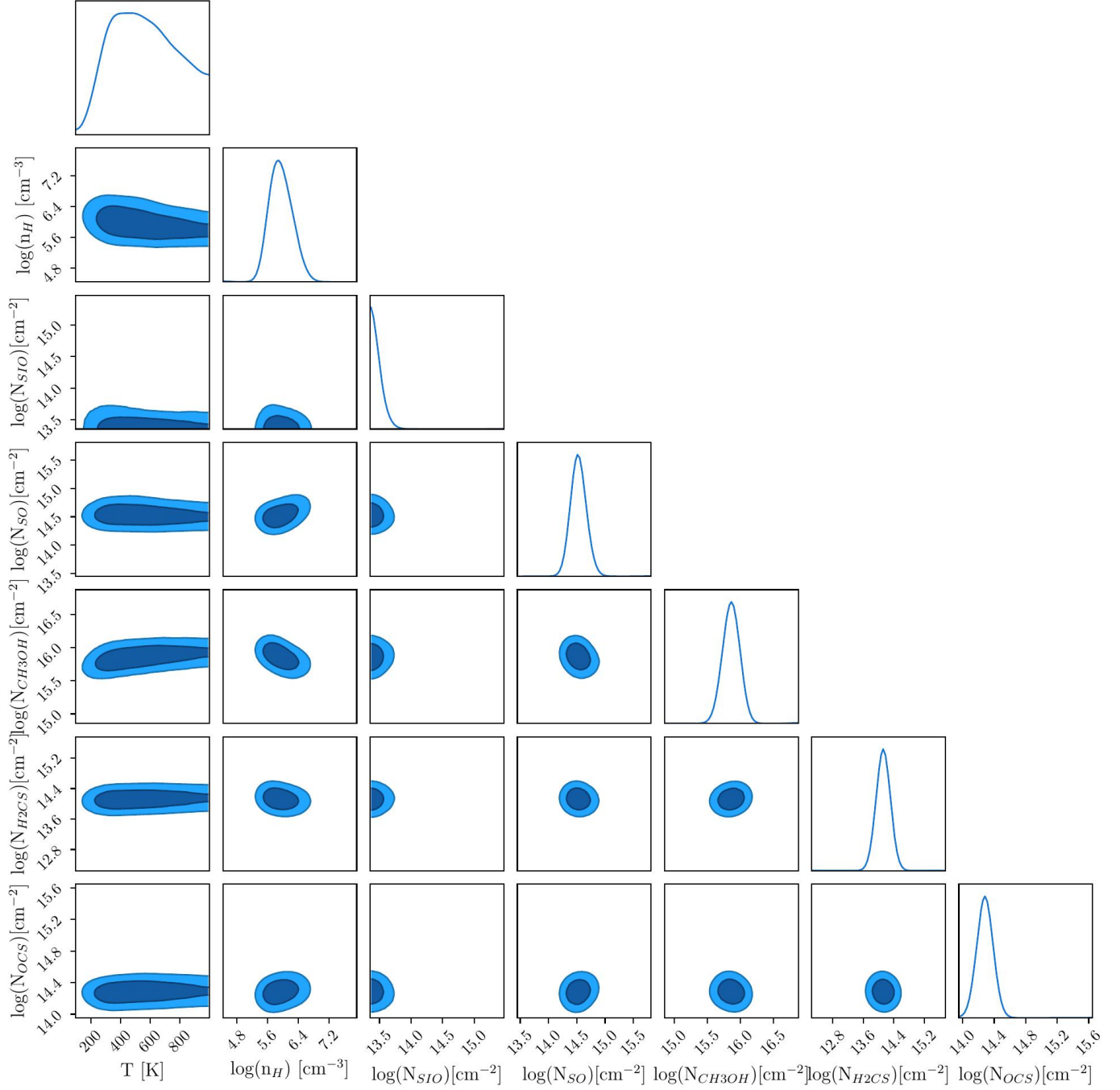


Figure 3. An example corner plot for the G2 source that shows the sampled distributions for each parameter, known as dimensions, in the model. Each dimension is shown on the x axis; the distributions on the diagonal represents the posterior distributions for the relevant dimension e.g. the posterior on the top left is the T posterior. All other plots in the matrix show the joint distributions of parameters as per their x and y axes that contribute to the associated posterior. Tight constraints are observed in the joint distributions within all dimensions except T which exhibits broad behaviour along its domain and highlights the broad errors associated with this dimension.

Within this matrix, the marginalised posterior distributions for each parameter are found on the diagonal. The peak of each of these distributions represents the point of highest posterior density (HPD) and it is this value that is taken to be the most likely model given the data. The plots found within the remaining cells represent the joint distributions for the parameters defined by their relevant x and y axes. Any pair of parameters that are bounded by a dark blue region is within 2σ of the HPD, whilst everything bounded within the light blue region is within 3σ of the HPD.

Considering the marginalised posterior distributions we see that each dimension peaks to a maximum, though not without a degree of skewness in the case of T . Inspecting the joint distributions of all dimensions except T shows roughly symmetrical, tight groupings that in general extend to ± 0.5 orders of magnitude. This produces posteriors that peak strongly, though both SiO and OCS peak towards the lower boundary of the distributions in this case.

Whilst estimates of T are broad, its HPD is reliably constrained in the case of $G2$. However, the skewness in this distribution does serve to highlight the asymmetrical errors that we find are often associated with this dimension. In this instance, the possible values $T < 350$ K become exponentially less likely. At $T > 350$ K we observe a small plateau of equal likelihood until $T \approx 600$ K, whereby an approximately linear decrease in likelihood until $T \approx 1000$ K is encountered.

Unfortunately, the large errors and associated systematic uncertainties in temperature are a consequence of the limited number of spectral lines detected and used in this analysis. In the majority of cases within this study we require fitting for at least 4 different dimensions using just 2 spectral lines. An example corner plot for this scheme is shown in Figure 4, which exhibits only SiO and SO lines. As a result, Figure 4 shows broader constraints in all dimensions and less symmetry in the posterior distributions therein, though T does peak despite 3σ errors spanning the entire parameter space. Subsequent inspection of the temperature column of Table 4 shows wide, asymmetrical errors on almost every constrained temperature, serving to highlight the challenge in drawing a discrete conclusion from a continuous, asymmetrical and weakly peaked distribution. The errors on each parameter become both smaller and more symmetrical in nature, when afforded more line detections, though the effect on constraining T is slight. Additionally, the broad temperature distributions may be reflective of the weak temperature dependence that is observed in the LAMDA collisional data for the detected molecular transitions. Further constraints could be ap-

plied if additional observations of molecular transitions that exhibit strong temperature dependent behaviour are incorporated.

6. INFERENCE RESULTS: GAS CONDITIONS IN THE CND

The derived HPD of the physical parameters for each position are shown in Figures 5 - 8. These plots are similar to that in Figure 2, however the colour scale employed to fill the apertures here is indicative of the HPD of the relevant dimension under consideration as computed from our inference routine. For instance, Figure 5 shows the HPD of gas temperature T_{kin} towards each observation. Similarly, Figures 6, 7 and 8 show the HPDs of n_{H} , N_{SiO} and N_{SO} respectively. Semi-transparent, hatched apertures represent sources that have not achieved reliable convergence within the maximum number of steps available. We define non-reliable convergence as any source that has converged to an HPD but without an associated 1σ error range. Table 4 within Appendix C shows the HPD for each source and each dimension therein together with their associated error ranges. Thus considering each image allows the dataset wide distribution of physical conditions to be investigated and quantified.

6.1. Temperature

The distribution of HPD temperatures T_{HPD} across the entirety of Figure 5 shows minor correlation on a local level; as expected, sources in close proximity to one another have broadly similar temperatures. In general, this behaviour manifests as ± 50 K between neighbouring sources. An example of this is found in Panel 1 which shows that $G3a$ and $G3b$ are almost identical in temperature of ≈ 100 K. Both $G3a$ and $G3b$, as well as $G1$ and $G2$, are found within a long filamentary structure of HCN emission that extends along the left vertical edge of Panel 1. This structure can be regarded as sitting outside of the main CND structure, and represents the 50 km s^{-1} molecular cloud identified in previous studies. However, both $G1$ and $G2$ are warmer than $G3a$ and $G3b$ with $T_{G1} \approx 350$ K and $T_{G2} \approx 600$ K. Additionally, Panel 1 also shows $G5$, which is external to the HCN filament. $G5$ is similar in temperature to $G3a$ and $G3b$ with $T_{G5} \approx 100$ K. There is also an unconstrained source on the boundary of the filament that is of similar temperature to $G3a$, $G3b$ and $G5$, though this source's temperature estimate is likely unreliable. Nevertheless, it would appear that the $G3a$ and $G3b$ observations capture the same gas component, whilst $G1$ and $G2$ capture colder and warmer extremes of the filament respectively.

When considering Panel 2, we see that the main grouping of observations in the centre of the panel are

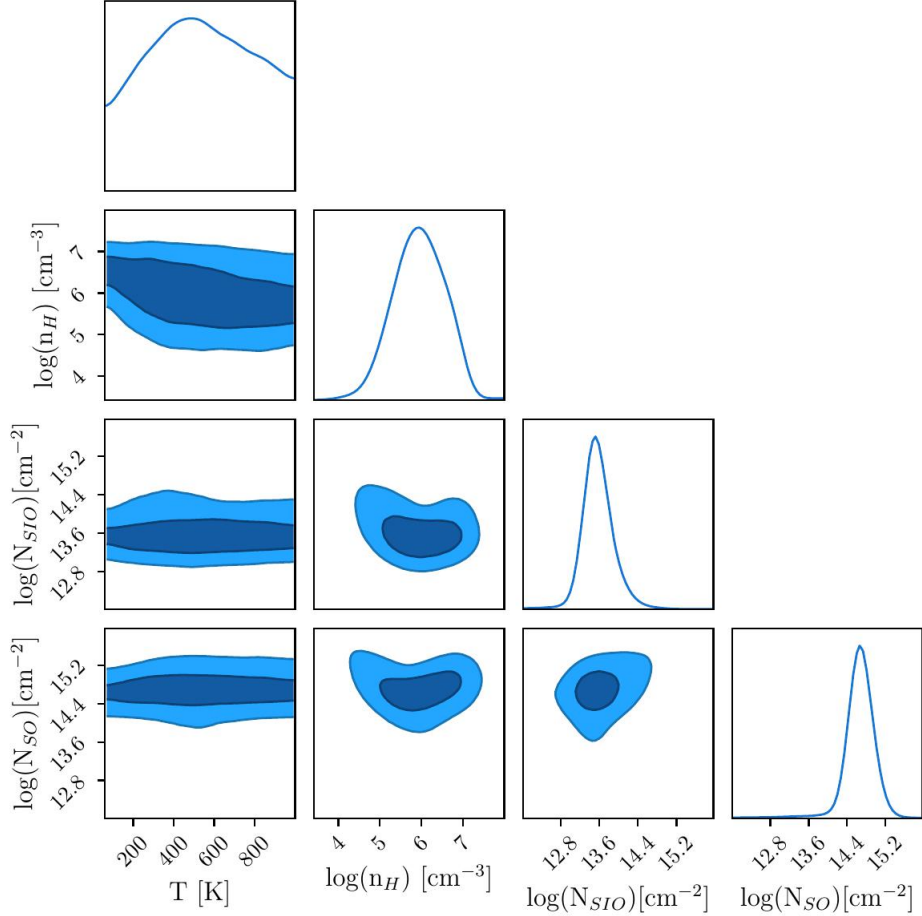


Figure 4. Corner plot for the K1 source as per Figure 3. This shows much broader spread in all dimensions owing to the limited number of data points available.

consistent with temperatures $400 < T_{\text{HPD}} < 700$ K, though there is a significant number of positions that have not achieved reliable temperature convergence. Additionally, 5 of the converged positions are identified as having $T_{\text{HPD}} \approx 500$ K. Interestingly, this is consistent with the bulk of the gas being close to the upper limit of the CNB clump temperature as identified by Requena-Torres et al. (2012). There are, however, 2 constrained “hot” sources within Panel 2 that exceed this limit: K15b and K24. Of these, K24 is the hottest at $T_{\text{K24}} \approx 800$ K, whilst K15b is moderately cooler at $T_{\text{K15b}} \approx 700$ K. K24 is isolated and much further North than K15b, and does not appear to correlate with the underlying HCN emission. Conversely, K15b sits embedded within the CNB and is much closer to cooler sources. This therefore indicates that in general the gas temperature is increasing towards the South of Panel 2 and, in turn, to the South of the CNB. This is also consistent with the underlying HCN emission becoming brighter towards the South of Panel 2.

Panel 3 shows a similar trend to that observed in the main grouping of Panel 2 in that almost every

source in Panel 3 has temperature within the range $350 < T_{\text{HPD}} < 550$ K. In this instance there are only 2 sources - L15 and L25 - that deviate significantly from ≈ 550 K. L25 sits at the furthest extremity of the observation grouping, whilst L15 sits centrally within that grouping. However, we observe that T_{HPD} increases from L15 along and down the line of observations towards L6, with L3 and L6 being of comparable temperature. The 2 sources either side of L6 - L10a and L1 - are again of comparable temperatures to L3 and L6. Continuing along and up from L15 towards L20 shows that the tight grouping of observations in L20, L21 and L24 are all of similar temperature, again $T_{\text{HPD}} \approx 550$ K. However, L25’s temperature of $T_{\text{HPD}} \approx 350$ K stands in contrast to its warmer surroundings.

Additionally, L19 is the observation that showed the largest $I_{\text{SiO}}/I_{\text{SO}}$ ratio in Panel 3 as well as globally across all observations. Panel 3 shows that its temperature is unconstrained, though if we consider the estimate in relation to its surroundings then we see no significant deviation from the average T_{HPD} of its surrounding observations.

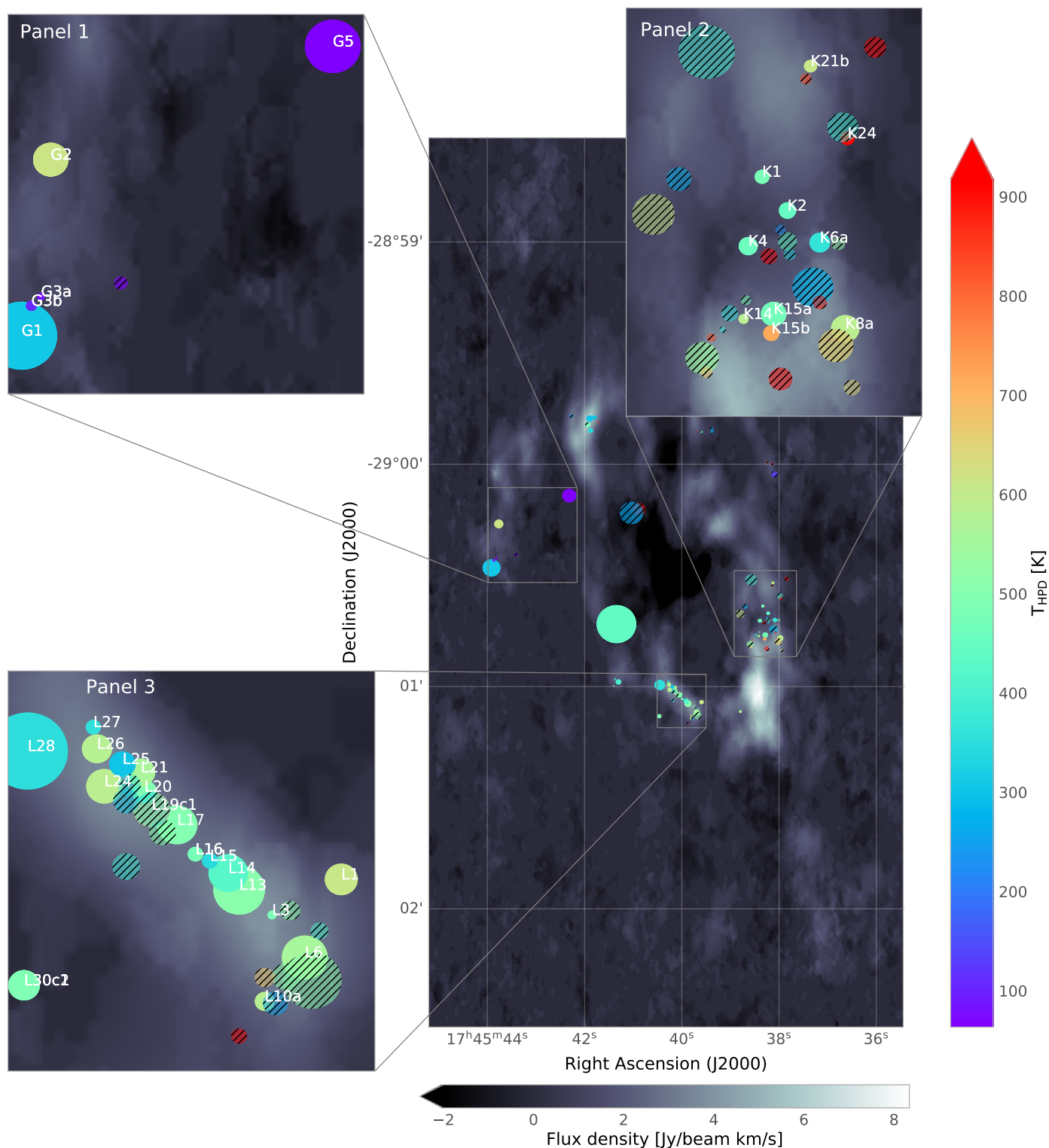


Figure 5. The points of highest posterior density (HPD) of the kinetic gas temperature T_{HPD} towards each position outlined in Section 2. Semi-transparent, hatched circular regions indicate a position whose chain has not reliably converged. G2 (in Panel 1) is noticeably warmer than its surroundings, which are much lower in their recovered temperatures. Panels 2 and 3 show more agreement between neighbouring positions.

6.2. Gas density

When considering the distribution of HPD densities n_{HPD} in Figure 6, we see a similar local trend to that observed in temperature in Figure 5 such that neighbouring sources are within 0.2 orders of magnitude of one another. Additionally, we also observe far fewer unconstrained sources than were noted in Figure 5. However, more uniformity is seen in the determined values of n_{HPD} throughout the CND as a whole, with less than 2 orders of magnitude variation throughout.

Panel 1 shows that, in general, colder sources are found to be at higher density. For example, G5 was identified as being ≈ 100 K and is, in turn, here noted to have density $n_{\text{G5}} \approx 10^7 \text{ cm}^{-3}$ - the most dense of any position in our sample. Whilst G1 and G2 were noted for their different temperatures (G1 becoming cooler than G2), Panel 1 shows that they are broadly similar in density within their associated error ranges. Furthermore the same density behaviour is seen in G3a, G3b and G4 which were all identified as having similar temperatures.

When considering Panel 2, almost every source sits within the range $10^{5.6} < n_{\text{HPD}} < 10^{6.2} \text{ cm}^{-3}$, even those outside of the main grouping identified in Panel 2 of Figure 5. The main grouping is found within an HCN bright region that defines the Southern extent of the CND. We note that the density range derived here is consistent with the density of HCN bright cores estimated by [Smith & Wardle \(2014\)](#). Additionally, the hot sources identified in K15b and K24 sit within this range and have densities $n_{\text{K15b}} \approx 10^{6.2} \text{ cm}^{-3}$ and $n_{\text{K24}} \approx 10^{5.8} \text{ cm}^{-3}$ respectively. K13a is identified as having a density towards the upper limit, i.e. $n_{\text{HPD}} \approx 10^{6.2} \text{ cm}^{-3}$, though its surroundings are of lesser density. When considered in conjunction with K9 and K10, it would appear that this region is tracing the dense inner-most ridge of the CND.

Outside of this grouping we identify that K18 exhibits a large density of $n_{\text{HPD}} \approx 10^{6.4} \text{ cm}^{-3}$. This is not consistent with the underlying HCN emission and is not reflected in the density of its nearest neighbour K19 whose density is $n_{\text{HPD}} \approx 10^{5.8} \text{ cm}^{-3}$. K18 is therefore regarded as an anomalous position.

Within Panel 3 we observe that the L16 source acts as a dividing boundary such that everything North of L16 - and thus the Northern-most cluster of observations - all exist at almost exactly the same density of $n_{\text{HPD}} \approx 10^{6.0} \text{ cm}^{-3}$. South of L16 we note that the sources show slightly more variety, with L3 being more dense than the average of $n_{\text{HPD}} > 10^{5.8} \text{ cm}^{-3}$ and L16 being less dense at $n_{\text{HPD}} > 10^{5.5} \text{ cm}^{-3}$. L12 is a unique outlier in that its density is significantly larger than any other source in Panel 3 at $n_{\text{HPD}} > 10^{6.4} \text{ cm}^{-3}$. Within Figure

5, L12 does not have a reliable temperature estimate. However, if we consider the temperature identified we observe that it is > 800 K, thus potentially forming another non-quiescent region.

Additionally, observations that sit within HCN regions or filaments are found to broadly exhibit higher densities than those observations outside of these locations. Given that HCN emission traces dense gas this is unsurprising, though it does lend additional weight to the hot, dense sources being embedded non-quiescent regions such as a YSO.

6.3. Column density

Much like Figure 6, the SiO column density in Figure 7 shows little variance across the dataset. Figure 7 shows just over an order of magnitude's variation. The effects of temperature and density also appear to be negligible in this case as the regional and local variation seen in Figures 5 and 6 are not observed, or indeed reflected, here. For example, Panel 1 in Figure 7 shows almost uniform N_{SiO} in the range $10^{13.4} > N_{\text{SiO}} < 10^{13.8} \text{ cm}^{-2}$ despite the temperature and density varying widely. A noticeable feature of Panel 1 is the additional uniformity in N_{SiO} for sources within the HCN filament. Sources outside of this filament, e.g. G5, are found to exhibit a different, larger column density.

Notable features within Panel 2 show that a tentative trend indicating the brighter the underlying HCN emission then the larger the SiO column density. For example, the upper half of the panel, where HCN emission is less intense, showing marginally lower column densities than the lower half where HCN emission is more intense. Curiously, K5a, K5b and K5c are observed to have lower column density of $N_{\text{SiO}} \approx 10^{13.3} \text{ cm}^{-2}$ than their surrounding observations. This could indicate that the surrounding gas acts to shield the K5 sources and thereby inhibit the emission of SiO. This is further confirmed when noting that the gas density of K5a, K5b and K5c are consistent with their surroundings. The lower half of Panel 2 is much more uniform of $N_{\text{SiO}} \approx 10^{13.6} \text{ cm}^{-2}$ with the exception of K8a which has column density $N_{\text{SiO}} \approx 10^{14.0} \text{ cm}^{-2}$. The inner CNR ridge (K9 to K13b) all show uniform and consistent column density of $N_{\text{SiO}} \approx 10^{13.6} \text{ cm}^{-2}$ with this agreement extending behind the ridge until K8a. Uniquely, the previously identified ridge indicated by K12, K13a and K13b shows no distinct SiO behaviour relative to its surroundings, thus indicating that any interaction between the Galactic Centre Mini Spiral and the CNR towards this region is not having an effect on the SiO chemistry.

Panel 3 is not dissimilar in broad trend to Panel 2 in that it shows the same agreement trends. The larger

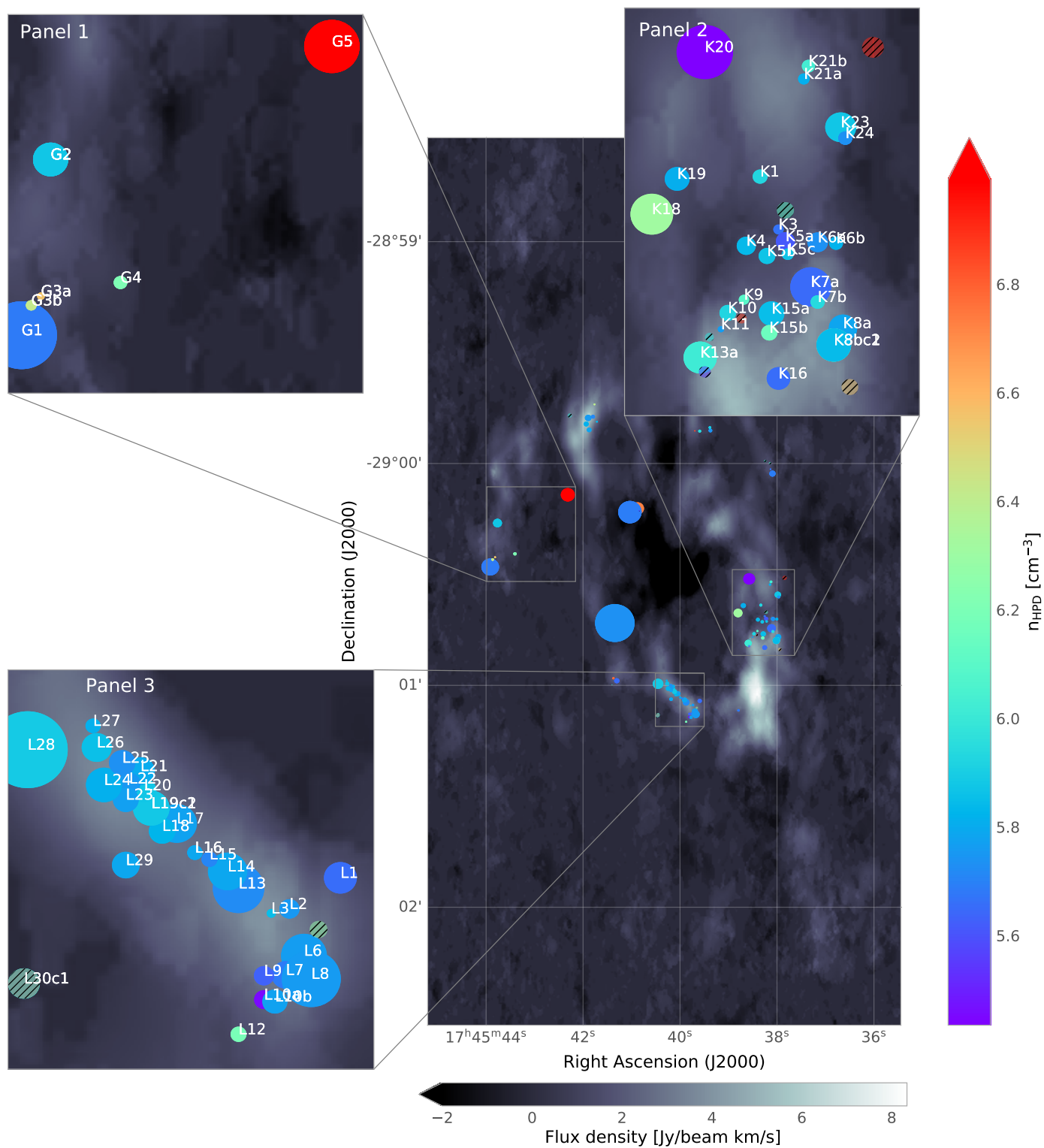


Figure 6. As per Figure 5, but here the colour of the circular regions represents Hydrogen gas density n_{H} towards each position outlined in Section 2. Again, semi-transparent, hatched circular regions indicate a source whose chain has not reliably converged.

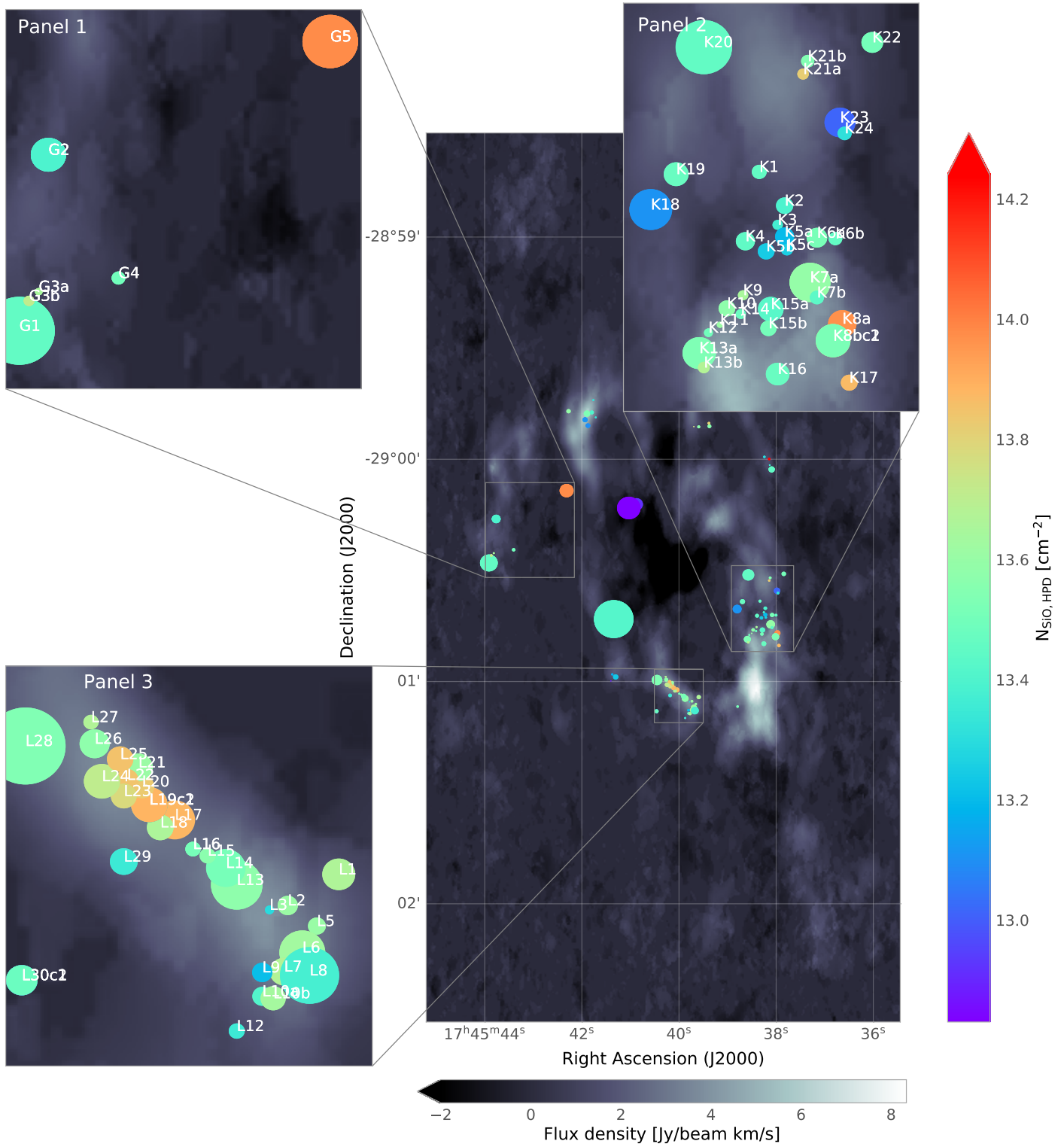


Figure 7. As per Figure 6, but here the colour of the circular regions represents SiO column density N_{SiO} towards each observation outlined in Section 2.

N_{SiO} is located towards the observation's Northernmost tip, with the column density decreasing towards the South of this complex. Interestingly, this region of relatively large N_{SiO} sits within an HCN dark region. By application, HCN traces dense molecular gas and thus shows that, at least in this region, that regions of large SiO column density are found in dense regions of gas.

Directly North of Panel 2 is another grouping of observations that houses the largest derived value of N_{SiO} at $\approx 10^{14.2} \text{ cm}^{-2}$. The surrounding observations are also observed to have N_{SiO} towards the upper-half of the derived scale, though these observations are consistent with the values of N_{SiO} derived towards the series of observations in Panels 2 and 3. This is again consistent with the underlying HCN emission tracing dense regions within the CNB, ergo grain-processing as described in Section 1.

Figure 8 shows that almost all sources can be considered to have $N_{\text{SO}} > 10^{14} \text{ cm}^{-2}$. A grouping of 3 observations immediately south of Sgr A* houses the lowest value of N_{SO} within our data at $\approx 10^{14} \text{ cm}^{-2}$.

Panel 1 echoes a similar trend to its SiO column densities, with the largest column density in this Panel - G5 - residing outside of the main HCN filament. Interestingly, G3b is here shown to be $N_{\text{SO}} \approx 10^{15} \text{ cm}^{-2}$, larger than it's surroundings in G1 and G2 that show consistent column densities of $N_{\text{SO}} > 10^{14.5} \text{ cm}^{-2}$. G3a and G4 are also consistent, with $N_{\text{SO}} > 10^{14.7} \text{ cm}^{-2}$.

Panel 2 again shows a number of interesting trends, specifically a degree of non-uniformity throughout the derived values in the main grouping. We observe that whilst the local agreement between neighbouring observations is again evident here, it is more evident in the upper half of the panel than in the lower half. For instance, the collection of sources from K1 to K6b all show $N_{\text{SO}} \approx 10^{14.8} \text{ cm}^{-2}$. To the South of this complex we find that the observations along the inner boundary ridge (K9 to K13b) of the CNB show large column densities towards K9 and K13b, with the column density in general decreasing towards the centre of this line towards K11. K8a also stands out as a high column density source, especially in relation to its lesser column density neighbours. However, the derived column densities for these sources span around 1 order of magnitude, making the individual variation from observation to observation slight. This is also true when applied to the interaction ridge, which is here observed to be less uniform than in SiO. However, this behaviour is consistent with the $I_{\text{SiO}}/I_{\text{SO}}$ ratio being consistent across the ridge.

Panel 3 again exhibits a similar trend to that seen in Figure 7, though there is even less variation in N_{SO} throughout this region. The HCN dark region towards

the Northernmost tip of this grouping may again be considered to house the largest values of $N_{\text{SO}} \approx 10^{15} \text{ cm}^{-2}$.

The dense N_{SiO} observation to the North of Panel 2 in Figure 7 now shows almost unanimous agreement in N_{SO} with its neighbours indicating that whatever mechanism is driving its excess SiO chemistry - relative to its surroundings - is not reflected in its SO chemistry.

When considering the trends in both Figures 7 and 8, we see variation in both N_{SiO} and N_{SO} throughout the data, though this variation is slight in both dimensions and likely not large enough to indicate any localised energetic events acting as vectors for excess emission in the vast majority of cases. Importantly, the derived SiO and SO column densities are larger than the expected quiescent column densities. The CNB wide nature of this enhancement suggests that the mechanism driving this excess is universal, and likely grain-processing and/or desorption.

7. FORMATION MECHANISMS

It is clear that all sources in our data show enhancement of SO and SiO. As already discussed, each of these molecules is a known tracer of grain-processing activity, owing to both Si and S being far more abundant on the grain surfaces than they are in the gas-phase. Indeed, SiO and SO do not form readily in the gas-phase without Si or S trapped in/on the grains being released in to the gas phase for subsequent reaction with O e.g. $\text{Si} + \text{O} \longrightarrow \text{SiO}$. Conversely, CH_3OH is thought to form readily on grain surfaces via successive hydrogenation of CO, where it is subsequently desorbed in to the gas-phase by an energetic mechanism such as shock activity (e.g. James et al. (2020)) or photodesorption (e.g. Bertin et al. (2016)).

Previous studies of the Galactic Center on large scales such as those by Molinari et al. (2011) and Yusef-Zadeh et al. (2013) have shown that the gas and dust are uncoupled and that the dust temperature $T_{\text{dust}} \leq 40 \text{ K}$, well below the temperature at which thermal desorption becomes significant. When considering smaller scales such as the CNB, Latvakoski et al. (1999) theorise that the dust temperature varies positionally from 40 K to 200 K, with the variation likely a result of heating by the OB star population. Furthermore, our analysis has also shown that the density of the most dense clumps to be $n_{\text{H}} \approx 10^7 \text{ cm}^{-3}$, a density at which the gas and dust are likely coupled, either fully or partially (Goldsmith 2001). As a result, thermal desorption could also be dominant within sub-regions of the CNB. This naturally poses the question: what physical event(s) are dominant in driving this grain-processing, and are these events associated with specific events such as star formation, or is it in-

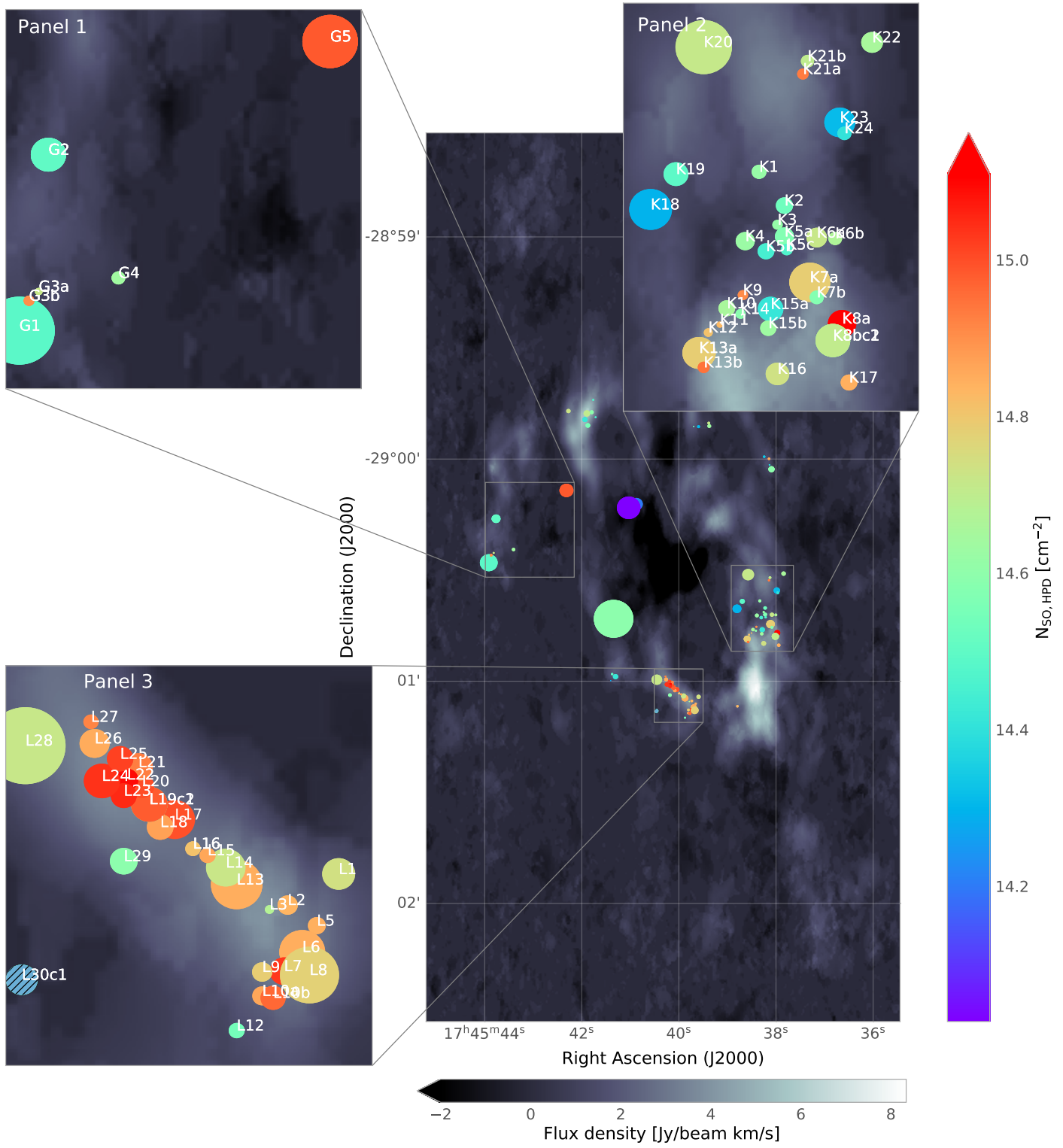


Figure 8. As per Figure 7, but here the colour of the circular regions represents SO column density N_{SO} towards each observation outlined in Section 2.

stead energetic activity associated with Sgr A* and its surroundings?

In the context of star formation, driven shock action is an efficient and ubiquitous processor of grains, so much so that molecules like SiO and SO are often used exclusively as tracers of shocks in star forming regions (Martin-Pintado et al. 1992; des Forêts et al. 1993). As already noted, the OB star population in the Central Cavity could raise the photoionisation rate towards the inner edge of the disc, making photodesorption of grain mantle species an efficient desorption mechanism here. Dense regions further in to the disc may also be subject to photodesorption via secondary photons. Crucially, such widespread desorption activity could act to pre-process the grain mantles, rendering molecules such as SiO and SO unreliable shock tracers in the CND.

Furthermore, the uniform enhancement of SiO and SO observed throughout our observations is indicative of a large scale process driving this desorption. Star formation would be expected to occur in a structured manner, to the extent that its signatures would be concentrated to relatively small regions of the CND. These signatures are dependent on the evolutionary state of the object; they could manifest as cold and dense self-gravitating regions, or hot and dense gas swept up in outflows.

K13a is, however, one of only 2 observations in our sample that shows significant OCS emission. K13a's surroundings do not exhibit similar OCS lines, indicating highly localised phenomena to the K13a locale. The only other OCS positive source is G2 which, unlike K13a, exhibits CH₃OH and H₂CS emission. Within K13a we note that the measured linewidth of the OCS line is a factor of 2 less than the measured linewidths of the SiO and SO lines. This is in spite of all lines towards K13a having consistent measured velocities. Such behaviour could indicate that the SiO and SO lines are tracing a different thermal component to the OCS line, hence we disregard the OCS line towards the position when fitting for K13a. As a result, the assumption of LTE should be cautioned towards this region.

Interestingly, when considering the G-pointing we find that G2 does not exhibit similar behaviour, though there is minor variation in measured linewidth across the detected lines. CH₃OH and H₂CS emission are widespread throughout the G pointing, creating a unique subset of observations within our sample. Unfortunately, the temperature towards K13a remains unconstrained. However, if we consider the point of highest posterior density towards K13a as absolute then $T_{K13a} \approx 500$ K. G2 has temperature $T_{G2} \approx 600$ K. As such, the presence of OCS could indicate high-temperature chemistry occurring within these regions. The non-detections of CH₃OH

and H₂CS in K13a is puzzling, though K13a is known to sit along the Galactic Center Mini Spiral - CND ridge and thus could be indicative of locally different chemistry. Conversely, OCS tracing a separate thermal component towards K13a, and the absence of this towards G2, potentially alludes to this interaction. Nevertheless, both of these regions require further chemical follow up study to confirm.

One may broadly estimate whether the derived conditions towards the positions in this study are indicative of star formation by considering density, mass and pressure estimates. Considering G2 we note that the Roche Density (Chandrasekhar 1987), assuming an approximate distance from Sgr A* of 3.0 pc, is $\approx 6 \times 10^6$ cm⁻³, which is marginally smaller than the derived gas density towards G2 thus implying tidal stability. Considering an estimate of the mass, assuming that G2 is spherical and uniform with average density $n_H \approx 10^6$ cm⁻³ and radius equivalent to ~ 3 beams we find its mass $M_{\text{uniform}} \approx 22 \times 10^3 M_{\odot}$. For G2 to be gravitationally bound with linewidth $\Delta v \approx 20$ km s⁻¹ then its mass would need to exceed the virial mass M_{vir} . Using the same process as Christopher et al. (2005), we find that M_{vir} towards G2 is $M_{\text{vir}} \approx 40 \times 10^3 M_{\odot}$, only marginally larger than M_{uniform} . As a result, G2 could very well be gravitationally bound within the limits of the assumptions applied. Additionally, another potentially bound source is L28 within the L pointing. L28 has uniform mass $M_{\text{uniform}} \approx 40 \times 10^3 M_{\odot}$ and virial mass $M_{\text{vir}} \approx 48 \times 10^3 M_{\odot}$, and shows the closest agreement between uniform and virial masses within our sample. For G5, we note $M_{\text{uniform}} \approx 1 \times 10^3 M_{\odot}$ and virial mass $M_{\text{vir}} \approx 4 \times 10^3 M_{\odot}$. However, the recovered gas density for G5 of $n_H \approx 10^7$ cm⁻³ is therefore larger than the equivalent Roche Density at 3.0 pc, implying that G5 could be able to overcome the tidal barrier to bind itself gravitationally. This assumes that G5 is one discrete, monolithic clump. Given that G5's physical conditions render it such an outlier amongst our observed regions, it is possible that this region is actually multiple clumps along the line of sight whose spectra sum to produce a single spectra, in turn creating the illusion of a spectra consistent with one unified clump.

We apply a similar process in order to estimate the total molecular gas mass contained within the CND. This can be expressed as $M_{\text{CND}} \approx \pi(R_{\text{out}}^2 - R_{\text{in}}^2)h\rho$ where h represents the height of the CND. Based on the underlying HCN maps in Figure 2 we assume that this is, on average, ≈ 0.5 pc. For comparison, we utilise the same CND radii reported in Tsuboi et al. (2018): $R_{\text{in}} \approx 1.5$ pc and $R_{\text{out}} \approx 2.0$ pc. Additionally, we assume that the average CND density is equivalent to the modal density

determined previously: $\approx 5 \times 10^5 \text{ cm}^{-3}$. This yields a total mass of $M_{\text{CND}} \approx 4 \times 10^4 M_{\odot}$. Tsuboi et al. (2018) estimate the molecular gas mass of the CND based on LTE assumptions to be $3 \times 10^4 M_{\odot}$, marginally smaller than our estimate. However, we caution that our observations do not sample the full extent of the CND, especially towards HCN faint regions such as those to the North of Sgr A*. In this instance, the use of the modal density derived from our observations - which deliberately target dense gas - could result in us overestimating the mean density of the CND, in turn biasing our mass estimate.

When considering both thermal and turbulent pressure, one may express the thermal pressure as $p_{\text{therm}}/k_B \approx nT$ and the turbulent pressure as $p_{\text{turb}}/k_B \approx \rho \Delta v^2/k_B$. For $T \approx 600 \text{ K}$, $n_{\text{H}} \approx 10^6 \text{ cm}^{-3}$ and $\Delta v \approx 20 \text{ km s}^{-1}$ then $p_{\text{therm}}/k_B \approx 10^9 \text{ cm}^{-3} \text{ K}$ and $p_{\text{turb}}/k_B \approx 10^{11} \text{ cm}^{-3} \text{ K}$. Therefore, for G2 the turbulent pressure dominates over the thermal pressure in spite of the high estimated temperature towards this region. In fact, all positions within the G, K and L pointings are dominated by turbulence, despite their wide range of estimated temperatures. Additionally, this is seemingly independent of their potentially bound states, though a more rigorous determination of mass based on LTE assumptions and chemical abundances is required to identify more accurate clump masses to compare to their virial counterparts.

8. CONCLUSIONS

In this paper, we have presented sub-arcsecond observations from 8 ALMA Band 7 (272 – 375 GHz) pointings towards the Circumnuclear disk (CND) of Sgr A*. We detect clear and distinct SiO ($8_7 - 7_6$) and SO ($7 - 6$) emission towards 98 positions within these pointings. Additionally, we observe widespread CH₃OH ($2_{1,1} - 2_{0,2}$) emission as well as more localised emission of H₂CS ($9_{1,9} - 8_{1,8}$) and OCS ($25 - 24$) towards a subset of these 98 positions.

We have used a Bayesian Inference routine coupled to radiative transfer to infer the physical conditions towards each observation based on the detected line fluxes. Based on these results, we find the following:

- The temperature of the regions probed by the observations is in general $T < 500 \text{ K}$, approximately consistent with that derived previously towards similar clumps. Most of the estimated densities within this work are in good agreement with the previously reported values towards clumps within the CND at $n_{\text{H}} \lesssim 10^6 \text{ cm}^{-3}$.

- The ubiquity of SiO and SO detections, including their large derived column densities, is consistent with large scale grain-processing occurring within the CND. However, we find that multiple desorption mechanisms, both thermal and non-thermal (e.g. UV or cosmic-ray photodesorption), are plausible engines with which to drive grain-processing in the CND. Further chemical modelling is required to identify which processes are efficient towards the CND.
- The G2 source within the Northeastern Arm is identified as being hot ($T_{\text{kin}} \approx 600 \text{ K}$) and dense ($n_{\text{H}} \approx 10^6 \text{ cm}^{-3}$). SiO ($8_7 - 7_6$) and SO ($7 - 6$) emission is identified towards it, as well as CH₃OH ($2_{1,1} - 2_{0,2}$), H₂CS ($9_{1,9} - 8_{1,8}$) and OCS ($25 - 24$) lines. Basic calculations indicate that this region is potentially gravitationally bound and is turbulent pressure dominated. It is therefore a source of immense interest for follow up observations and study.
- L28 is identified as having mass almost exactly consistent with that required for binding to occur, though turbulence dominates here as well. L28 does not show any outstanding feature in terms of its line detections or its recovered physical quantities, rendering it somewhat of an outlier amongst the potentially bound sources identified. Nevertheless, more accurate mass estimates in follow up studies based on complex chemistry can help constrain whether this region is indeed bound or not.
- Similarly, G5 is found to have the largest recovered density within our data of $n_{\text{H}} \approx 10^7 \text{ cm}^{-3}$ whilst also exhibiting one of the lowest recovered temperatures at $T_{\text{kin}} \approx 60 \text{ K}$. G5's high density is sufficient to overcome tidal effects prohibiting the object from being gravitational bound. Basic mass estimates also support this finding.
- Another position of chemical interest is K13a. K13a shows detections of SiO ($8_7 - 7_6$) and SO ($7 - 6$) as well as OCS ($25 - 24$) - the only other position other than G2 to exhibit the OCS line. K13a is located along a ridge of the CND that is interacting with the Galactic Centre Mini Spiral. Further follow up study is required to understand the role that the ionised gas within the Galactic Centre Mini Spiral plays in the chemistry of this ridge.
- Using a similar mass derivation approach, we find that the total molecular gas mass contained within

the CND between 1.5 - 2.0 pc is $M_{\text{CND}} \approx 4 \times 10^4 M_{\odot}$.

ACKNOWLEDGMENTS

TAJ is funded by an STFC studentship, and thanks the STFC accordingly. SV acknowledges the European Research Council (ERC) Advanced Grant MOPPEX 833460 as well as the European Union’s Horizon 2020 research and innovation program under the Marie Skłodowska-Curie grant agreement No. 811312 for the project “Astro-Chemical Origins” (ACO). We thank J. Holdship for their discussion, opinions and associated improvements on aspects of this work. We also thank the anonymous referee and editors for their comments,

suggestions and improvements that have enriched and clarified this work. This paper makes use of the following ALMA data: ADS/JAO.ALMA#2013.1.01242.S. ALMA is a partnership of ESO (representing its member states), NSF (USA) and NINS (Japan), together with NRC (Canada), MOST and ASIAA (Taiwan), and KASI (Republic of Korea), in cooperation with the Republic of Chile. The Joint ALMA Observatory is operated by ESO, AUI/NRAO and NAOJ.

Software: emcee (Foreman-Mackey et al. 2013), ChainConsumer (Hinton 2016), RADEX (Van Der Tak et al. 2007), CASA (4.7.0; McMullin et al. 2007)

REFERENCES

- Abuter, R., Amorim, A., Bauböck, M., et al. 2019, *Astronomy & Astrophysics*, 625, L10, doi: [10.1051/0004-6361/201935656](https://doi.org/10.1051/0004-6361/201935656)
- Amo-Baladrón, M. A., Martín-Pintado, J., & Martín, S. 2011, *A&A*, 526, 54, doi: [10.1051/0004-6361/200913545](https://doi.org/10.1051/0004-6361/200913545)
- Armijos-Abendaño, J., Banda-Barragán, W. E., Martín-Pintado, J., et al. 2020, *Monthly Notices of the Royal Astronomical Society*
- Bertin, M., Romanzin, C., Doronin, M., et al. 2016, *The Astrophysical Journal Letters*, 817, L12, doi: [10.3847/2041-8205/817/2/L12](https://doi.org/10.3847/2041-8205/817/2/L12)
- Beuther, H., Zhang, Q., Bergin, E. A., & Sridharan, T. K. 2008, *The Astronomical Journal*, 137, 406, doi: [10.1088/0004-6256/137/1/406](https://doi.org/10.1088/0004-6256/137/1/406)
- Bradford, C. M., Stacey, G. J., Nikola, T., et al. 2005, *The Astrophysical Journal*, 623, 866
- Brooks, S. P., & Gelman, A. 1998, *Journal of Computational and Graphical Statistics*, 7, 434
- Chandrasekhar, S. 1987, *Ellipsoidal figures of equilibrium* (New York : Dover, 1987). <https://ui.adsabs.harvard.edu/abs/1987efe..book.....C/abstract>
- Christopher, M. H., Scoville, N. Z., Stolovy, S. R., & Yun, M. S. 2005, *The Astrophysical Journal*, 622, 346, doi: [10.1086/427911](https://doi.org/10.1086/427911)
- Ciurlo, A., Campbell, R. D., Morris, M. R., et al. 2020, *Nature*, 337, <https://www.nature.com/articles/s41586-019-1883-y>
- des Forêts, G., Roueff, E., Schilke, P., & Flower, D. R. 1993, *Monthly Notices of the Royal Astronomical Society*, 262, 915, doi: [10.1093/mnras/262.4.915](https://doi.org/10.1093/mnras/262.4.915)
- Eckart, A., Moultaqa, J., Viehmann, T., Straubmeier, C., & Mouawad, N. 2004, *The Astrophysical Journal*, 602, 760
- Ekers, R. D., van Gorkom, J. H., Schwarz, U. J., & Goss, W. M. 1983, *Astronomy & Astrophysics*, 122, 143
- Flower, D. R., Le Bourlot, J., Pineau, G., et al. 2003, *Astrophysics and Space Science*, 287, 183, doi: [10.1023/B:ASTR.0000006221.18403.18](https://doi.org/10.1023/B:ASTR.0000006221.18403.18)
- Foreman-Mackey, D., Hogg, D. W., Lang, D., & Goodman, J. 2013, *Publications of the Astronomical Society of the Pacific*, 125, 306. <http://dan.iel.fm/emcee>.
- Gelman, A., & Rubin, D. B. 1991, in *Fourth Valencia International Meeting on Bayesian Statistics*
- Genzel, R., Eisenhauer, F., & Gillessen, S. 2010, *The Galactic Center Massive Black Hole and Nuclear Star Cluster*, Tech. rep., Max-Planck Institut für Extraterrestrische Physik, Garching
- Genzel, R., Thatte, N., Krabbe, A., Kroker, H., & Tacconi-Garman, L. E. 1996, *The Astrophysical Journal*, 472, 153, doi: [10.1086/178051](https://doi.org/10.1086/178051)
- Ghez, A. M., Salim, S., Hornstein, S. D., et al. 2005, *The Astrophysical Journal*, 620, 744
- Gillessen, S., Eisenhauer, F., Trippe, S., et al. 2009, *The Astrophysical Journal*, 692, 1075, doi: [10.1088/0004-637X/692/2/1075](https://doi.org/10.1088/0004-637X/692/2/1075)
- Goldsmith, P. F. 2001, *THE ASTROPHYSICAL JOURNAL*, 557, 736
- Goto, M., Indriolo, N., Geballe, T. R., & Usuda, T. 2013, *Journal of Physical Chemistry A*, 117, 9919, doi: [10.1021/jp400017s](https://doi.org/10.1021/jp400017s)
- Gottlieb, C. A., Ball, J. A., Gottlieb, E. W., & Dickinson, D. F. 1979, *The Astrophysical Journal*, 227, 422
- Guesten, R., Genzel, R., Wright, M. C. H., et al. 1987, *The Astrophysical Journal*, 318, 124, doi: [10.1086/165355](https://doi.org/10.1086/165355)
- Harada, N., Riquelme, D., Viti, S., et al. 2015, *A&A*, 584, 102, doi: [10.1051/0004-6361/201526994](https://doi.org/10.1051/0004-6361/201526994)
- Hinton, S. R. 2016, *The Journal of Open Source Software*, 1, 45, doi: [10.21105/joss.00045](https://doi.org/10.21105/joss.00045)

- Holdship, J., Viti, S., Jiménez-Serra, I., Makrymallis, A., & Priestley, F. 2017, *The Astronomical Journal*, doi: [10.3847/1538-3881/aa773f](https://doi.org/10.3847/1538-3881/aa773f)
- Jackson, J. M., Geis, N., Genzel, R., et al. 1993, *The Astrophysical Journal*, 402, , doi: [10.1086/172120](https://doi.org/10.1086/172120)
- James, T. A., Viti, S., Holdship, J., & Jiménez-Serra, I. 2020, *Astronomy and Astrophysics*, 634, doi: [10.1051/0004-6361/201936536](https://doi.org/10.1051/0004-6361/201936536)
- Jones, P. A., Burton, M. G., Cunningham, M. R., et al. 2011, *Mon. Not. R. Astron. Soc.*, 000, 1. <http://www.atnf.csiro.au/people/mcalabre/livedata.html>
- Lacy, J. H., Townes, C. H., Geballe, T. R., & Hollenbach, D. J. 1980, *The Astrophysical Journal*, 241, 132, doi: [10.1086/158324](https://doi.org/10.1086/158324)
- Latvakoski, H. M., Stacey, G. J., Gull, G. E., & Hayward, T. L. 1999, *THE ASTROPHYSICAL JOURNAL*, 511, 761
- Lau, R. M., Herter, T. L., Morris, M. R., Becklin, E. E., & Adams, J. D. 2013, *The Astrophysical Journal*, 775, 37, doi: [10.1088/0004-637x/775/1/37](https://doi.org/10.1088/0004-637x/775/1/37)
- Lique, F., Van Der Tak, F. F. S., Klos, J., Bulthuis, J., & Alexander, M. H. 2009, *A&A*, 493, 557, doi: [10.1051/0004-6361:200810453](https://doi.org/10.1051/0004-6361:200810453)
- Lu, J. R., Ghez, A. M., Hornstein, S. D., et al. 2008, *The Astrophysical Journal*, 690, 1463, doi: [10.1088/0004-637/690/2/1463](https://doi.org/10.1088/0004-637/690/2/1463)
- Martin, S., Martin-Pintado, J., Montero-Castaño, M., Ho, P. T. P., & Blundell, R. 2012, *\aap*, 539, A29, doi: [10.1051/0004-6361/201117268](https://doi.org/10.1051/0004-6361/201117268)
- Martin-Pintado, J., Bachiller, R., & Fuente, A. 1992, *Astronomy & Astrophysics*, 254, 315
- Mauerhan, J. C., Cotera, A., Dong, H., et al. 2010, *The Astrophysical Journal*, 725, 188, doi: [10.1088/0004-637X/725/1/188](https://doi.org/10.1088/0004-637X/725/1/188)
- McMullin, J. P., Waters, B., Schiebel, D., Young, W., & Golap, K. 2007, *Astronomical Data Analysis Software and Systems XVI ASP Conference Series*, 376, 127. <http://casa.nrao.edu>
- Mills, E. A. C., Güsten, R., Requena-Torres, M. A., & Morris, M. R. 2013, *The Astrophysical Journal*, 779, 47, doi: [10.1088/0004-637X/779/1/47](https://doi.org/10.1088/0004-637X/779/1/47)
- Molinari, S., Bally, J., Noriega-Crespo, A., et al. 2011, *Astrophysical Journal Letters*, 735, doi: [10.1088/2041-8205/735/2/L33](https://doi.org/10.1088/2041-8205/735/2/L33)
- Montero-Castaño, M., Herrnstein, R. M., & Ho, P. T. P. 2009, *The Astrophysical Journal*
- Paumard, T., Genzel, R., Martins, F., et al. 2006, *The Astrophysical Journal*, 643, 1011, doi: [10.1086/503273](https://doi.org/10.1086/503273)
- Remijan, A. J., Markwick-Kemper, A., & ALMA Working Group on Spectral Line Frequencies. 2007, in *American Astronomical Society Meeting Abstracts*, Vol. 211, American Astronomical Society Meeting Abstracts, 132.11
- Requena-Torres, M. A., Güsten, R., Weiß, A., et al. 2012, *Astronomy & Astrophysics*. <http://www.iram.fr/IRAMFR/GILDAS>
- Schöier, F., van der Tak, F., van Dishoeck, E., & Black, J. 2010, *LAMDA: Leiden Atomic and Molecular Database*
- Smith, I. L., & Wardle, M. 2014, *Monthly Notices of the Royal Astronomical Society*, 437, 3159, doi: [10.1093/mnras/stt2092](https://doi.org/10.1093/mnras/stt2092)
- Smith, M. D., & Mac Low, M.-M. 2014, *ASTRONOMY AND ASTROPHYSICS*. <https://arxiv.org/abs/9703171v1>
- Tsuboi, M., Kitamura, Y., Uehara, K., et al. 2018, *Publications of the Astronomical Society of Japan*, 70, doi: [10.1093/pasj/psy080](https://doi.org/10.1093/pasj/psy080)
- Turner, B. E. 1998, *The Astrophysical Journal*, 501, 731, doi: [10.1086/305859](https://doi.org/10.1086/305859)
- Van Der Tak, F. F. S., Black, J. H., Schöier, F. L., Jansen, D. J., & Van Dishoeck, E. F. 2007, *A&A*, 468, 627, doi: [10.1051/0004-6361:20066820](https://doi.org/10.1051/0004-6361:20066820)
- Van Dishoeck, E. F., Kristensen, L. E., Mottram, J. C., et al. 2021, *Astronomy & Astrophysics*
- Wirström, E. S., Bergman, P., Black, J. H., et al. 2010, *A&A*, 522, 19, doi: [10.1051/0004-6361/200913766](https://doi.org/10.1051/0004-6361/200913766)
- Wright, M. C. H., Coil, A. L., McGary, R. S., Ho, P. T. P., & Harris, A. I. 2001, *\apj*, 551, 254, doi: [10.1086/320089](https://doi.org/10.1086/320089)
- Yusef-Zadeh, F., Cotton, W., Viti, S., Wardle, M., & Royster, M. 2013, *The Astrophysical Journal Letters*, 764, 19, doi: [10.1088/2041-8205/764/2/L19](https://doi.org/10.1088/2041-8205/764/2/L19)
- Yusef-Zadeh, F., Muno, M., Wardle, M., & Lis, D. C. 2007, *The Astrophysical Journal*, 656, 847, doi: [10.1086/510663](https://doi.org/10.1086/510663)
- Yusef-Zadeh, F., Roberts, D. A., Goss, W. M., Frail, D. A., & Green, A. J. 1999, *The Astrophysical Journal*, 512, 230, doi: [10.1086/306769](https://doi.org/10.1086/306769)
- Yusef-Zadeh, F., Wardle, M., Kunneriath, D., et al. 2017, *The Astrophysical Journal*, 850, L30, doi: [10.3847/2041-8213/aa96a2](https://doi.org/10.3847/2041-8213/aa96a2)

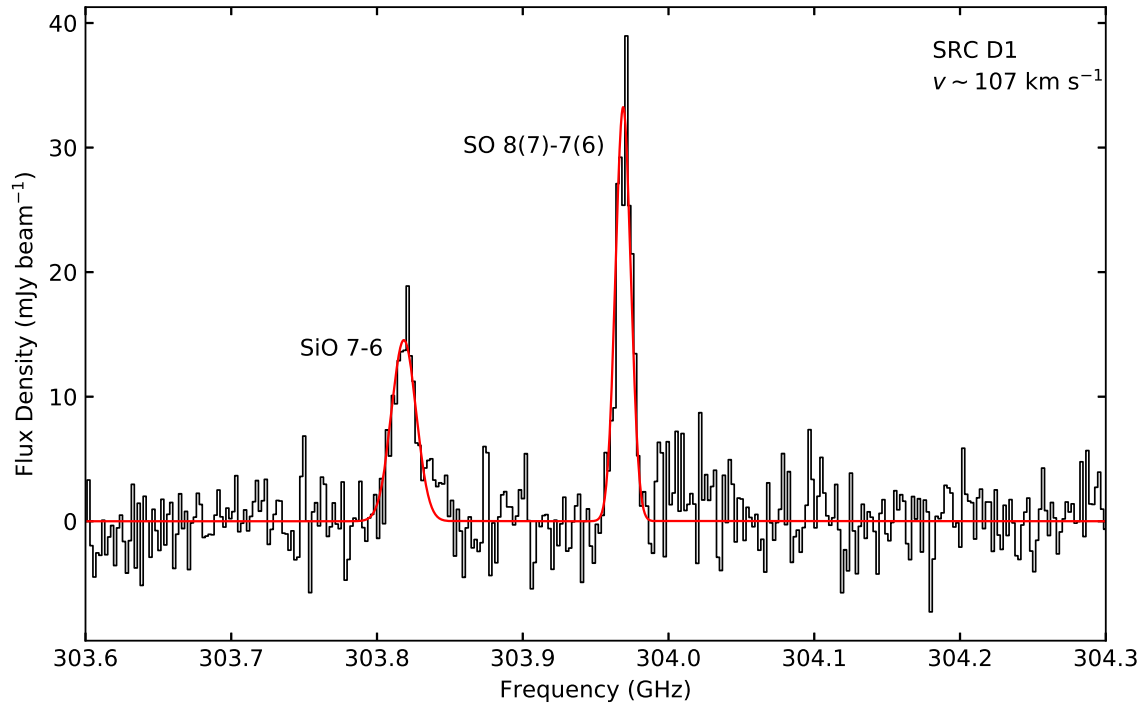


Figure 9. An example individual spectra for position D1. Spectra for each position in which at least one line was identified are available in the online journal.

APPENDIX

A. INDIVIDUAL SPECTRA

Fig. Set 9. Individual spectra

B. TABULATED SPECTRAL DATA

Table 3. Tabulated summary of observations including the source designation, its RA and Dec, extent in beam sizes, the emission line detected, its peak line flux density, the local standard of rest velocity, the linewidth and the ratio of SiO to SO flux densities where relevant.

Source	α (J2000)	δ (J2000)	Extent (beam)	Emission Line	Flux density (mJy/beam)	v (km s ⁻¹)	Δv (km s ⁻¹)	$I_{\text{SiO}}/I_{\text{SO}}$
N3	17 ^h 45 ^m 40.62 ^s	-29°00'24.05''	1.00	SiO 7-6	58.6 ± 3.6	-25.56	27.6	
IRS7	17 ^h 45 ^m 40.04 ^s	-29°00'22.76''	1.00	SO 8(7)-7(6)	8.34 ± 2.6	32.80	20.9	
N8	17 ^h 45 ^m 40.85 ^s	-29°00'12.88''	1.00	SiO 7-6	11.4 ± 5.3	39.52	11.8	0.56 ± 0.28
				SO 8(7)-7(6)	20.5 ± 4.1	38.73	15.0	
N7a	17 ^h 45 ^m 40.88 ^s	-29°00'12.23''	10.65	SiO 7-6	4.31 ± 0.47	41.23	13.9	0.56 ± 0.07
				SO 8(7)-7(6)	7.66 ± 0.40	40.1649	16.2	
N7b	17 ^h 45 ^m 41.04 ^s	-29°00'13.24''	19.59	SiO 7-6	3.7 ± 0.22	39.33	13.9	0.67 ± 0.05
				SO 8(7)-7(6)	5.53 ± 0.20	41.1081	15.5	
C1	17 ^h 45 ^m 41.35 ^s	-29°00'43.23''	33.03	CH ₃ OH 2(1,1)-2(0,2)	2.43 ± 0.36	37.68	8.68	0.48 ± 0.03
				SiO 7-6	8.13 ± 0.35	-42.7327	24.8	
G1	17 ^h 45 ^m 43.92 ^s	-29°00'28.07''	14.8	SO 8(7)-7(6)	17.0 ± 0.47	-42.5732	18.6	0.88 ± 0.08
				SiO 7-6	5.84 ± 0.42	67.47	35.4	
G2	17 ^h 45 ^m 43.77 ^s	-29°00'16.19''	73.6	SO 8(7)-7(6)	7.77 ± 0.5	64.58	30.3	0.75 ± -0.01
				CH ₃ OH 2(1,1)-2(0,2)	4.49 ± 0.47	59.29	31.7	
G3a	17 ^h 45 ^m 43.82 ^s	-29°00'25.43''	1.59	SiO 7-6	9.53 ± 0.10	56.84	19.7	0.92 ± 0.15
				SO 8(7)-7(6)	16.7 ± 0.13	55.64	-15.0	
G3b	17 ^h 45 ^m 43.87 ^s	-29°00'26.05''	2.24	CH ₃ OH 2(1,1)-2(0,2)	9.57 ± 0.12	56.14	15.6	0.68 ± 0.08
				H ₂ CS 9(1,9)-8(1,8)	6.6 ± 0.19	54.66	9.99	
G3b	17 ^h 45 ^m 43.87 ^s	-29°00'26.05''	2.24	OCS 25-24	1.72 ± 0.16	54.34	12.5	0.68 ± 0.08
				SiO 7-6	32.2 ± 3.8	53.65	9.86	
G3b	17 ^h 45 ^m 43.87 ^s	-29°00'26.05''	2.24	SO 8(7)-7(6)	39.2 ± 4.3	52.77	8.82	0.68 ± 0.08
				CH ₃ OH 2(1,1)-2(0,2)	29.1 ± 3.9	54.01	9.7	
G3b	17 ^h 45 ^m 43.87 ^s	-29°00'26.05''	2.24	H ₂ CS 9(1,9)-8(1,8)	21.2 ± 4.4	53.24	8.42	0.68 ± 0.08
				SiO 7-6	35.1 ± 3.5	56.66	10.6	
G3b	17 ^h 45 ^m 43.87 ^s	-29°00'26.05''	2.24	SO 8(7)-7(6)	48.6 ± 3.3	56.98	11.2	0.68 ± 0.08
				CH ₃ OH 2(1,1)-2(0,2)	22.5 ± 3.0	57.15	12.2	
G3b	17 ^h 45 ^m 43.87 ^s	-29°00'26.05''	2.24	H ₂ CS 9(1,9)-8(1,8)	16.4 ± 3.7	55.51	10.1	

Source	α (J2000)	δ (J2000)	Extent (beam)	Emission Line	Flux density (mJy/beam)	v (km s ⁻¹)	Δv (km s ⁻¹)	$I_{\text{SiO}}/I_{\text{SO}}$	
G4	17 ^h 45 ^m 43.41 ^s	-29°00'24.51''	2.85	SiO 7-6	20.3 ± 3.1	52.59	11.2	0.72 ± 0.13	
				SO 8(7)-7(6)	25.7 ± 2.8	53.18	12.3		
				CH ₃ OH 2(1,1)-2(0,2)	14.5 ± 2.7	52.37	13.0		
G5	17 ^h 45 ^m 42.32 ^s	-29°00'8.55''	11.6	SiO 7-6	39.0 ± 4.7	55.18	15.5	0.93 ± 0.15	
				SO 8(7)-7(6)	36.1 ± 4.0	56.19	18.1		
				CH ₃ OH 2(1,1)-2(0,2)	39.9 ± 4.9	54.99	14.9		
				H ₂ CS 9(1,9)-8(1,8)	17.6 ± 5.3	55.48	13.8		
D1	17 ^h 45 ^m 42.28 ^s	-28°59'47.11''	3.69	SiO 7-6	14.5 ± 1.4	107.1	19.6	0.7 ± 0.08	
				SO 8(7)-7(6)	33.2 ± 2.2	107.5	12.2		
D2	17 ^h 45 ^m 41.90 ^s	-28°59'47.76''	5.52	SiO 7-6	14.4 ± 0.7	106.3	17.3	0.65 ± 0.04	
				SO 8(7)-7(6)	25.4 ± 0.8	106.0	15.1		
D3c1	17 ^h 45 ^m 41.94 ^s	-28°59'49.41''	4.2	SiO 7-6	4.61 ± 0.58	109.8	21.3	0.55 ± 0.08	
					4.51 ± 0.6	75.89	20.5		0.46 ± 0.07
				SO 8(7)-7(6)	11.2 ± 0.77	108.0	15.8		
					9.55 ± 0.59	76.10	21.1		
D4	17 ^h 45 ^m 41.80 ^s	-28°59'47.44''	3.3	SiO 7-6	16.3 ± 1.3	107.31	11.7	0.62 ± 0.06	
				SO 8(7)-7(6)	23.3 ± 1.2	106.34	13.2		
				CH ₃ OH 2(1,1)-2(0,2)	6.53 ± 1.4	107.233	11.0 &		
D5	17 ^h 45 ^m 41.88 ^s	-28°59'51.00''	4.04	SiO 7-6	4.75 ± 0.74	77.92	18.8	0.33 ± 0.05	
				SO 8(7)-7(6)	12.1 ± 0.63	76.81	22.1		
D6	17 ^h 45 ^m 41.72 ^s	-28°59'48.78''	1.63	SiO 7-6	15.5 ± 3.1	-12.20	9.44	0.71 ± 0.17	
				SO 8(7)-7(6)	12.9 ± 1.8	-14.01	15.9		
D7	17 ^h 45 ^m 41.77 ^s	-28°59'44.10''	1.65	SiO 7-6	10.9 ± 2.2	93.44	13.3	0.67 ± 0.16	
				SO 8(7)-7(6)	19.5 ± 2.6	93.69	11.1		
H1a	17 ^h 45 ^m 39.38 ^s	-28°59'51.18''	3.1	SiO 7-6	18.4 ± 1.1	35.10	14.7	0.83 ± 0.07	
				SO 8(7)-7(6)	25.6 ± 1.3	34.95	12.7		
				CH ₃ OH 2(1,1)-2(0,2)	4.96 ± 0.88	35.74	19.3		
H1b	17 ^h 45 ^m 39.39 ^s	-28°59'50.36''	2.3	SiO 7-6	22.3 ± 1.1	30.53	21.7	1.24 ± 0.1	
				SO 8(7)-7(6)	18.2 ± 1.1	30.61	21.4		
				CH ₃ OH 2(1,1)-2(0,2)	6.49 ± 1.3	28.36	17.2		
H2	17 ^h 45 ^m 39.60 ^s	-28°59'51.33''	2.6	SiO 7-6	17.5 ± 1.7	37.15	15.6	1.85 ± 0.37	
				SO 8(7)-7(6)	12.6 ± 2.2	36.92	11.7		
H3	17 ^h 45 ^m 39.70 ^s	-28°59'51.26''	1.1	SiO 7-6	14.2 ± 1.7	53.01	28.2	1.78 ± 0.43	
				SO 8(7)-7(6)	10.3 ± 2.2	48.21	21.9		
H4	17 ^h 45 ^m 39.76 ^s	-28°59'46.03''	2.11	SiO 7-6	13.5 ± 0.97	73.59	32.9	2.04 ± 0.34	
				SO 8(7)-7(6)	7.24 ± 1.1	70.22	30.1		
J1	17 ^h 45 ^m 38.14 ^s	-29°00'1.65''	1.3	SiO 7-6	14.3 ± 2.9	62.28	11.3	0.95 ± 0.27	
				SO 8(7)-7(6)	18.5 ± 3.6	60.90	9.23		
				CH ₃ OH 2(1,1)-2(0,2)	8.42 ± 2.4	60.49	13.7		
				H ₂ CS 9(1,9)-8(1,8)	6.57 ± 1.9	60.76	17.5		

Source	α (J2000)	δ (J2000)	Extent (beam)	Emission Line	Flux density (mJy/beam)	v (km s ⁻¹)	Δv (km s ⁻¹)	$I_{\text{SiO}}/I_{\text{SO}}$	
J2	17 ^h 45 ^m 38.15 ^s	-29°00'0.01''	2.2	SiO 7-6	46.9 ± 1.0	67.16	27.5	2.26 ± 0.12	
				SO 8(7)-7(6)	25.0 ± 1.2	65.70	22.8		
J3	17 ^h 45 ^m 38.10 ^s	-29°00'2.82''	5.2	SiO 7-6	14.6 ± 0.81	75.19	14.3	0.67 ± 0.04	
				SO 8(7)-7(6)	25.5 ± 0.94	74.50	12.3		
				CH ₃ OH 2(1,1)-2(0,2)	10.2 ± 0.87	73.31	13.3		
				H ₂ CS 9(1,9)-8(1,8)	6.13 ± 1.6	75.00	7.43		
J4	17 ^h 45 ^m 38.25 ^s	-28°59'59.44''	2.06	SiO 7-6	10.3 ± 2.2	68.63	12.7	0.88 ± 0.25	
				SO 8(7)-7(6)	14.6 ± 2.8	68.91	10.2		
				CH ₃ OH 2(1,1)-2(0,2)	10.8 ± 4.4	67.94	6.46		
K1	17 ^h 45 ^m 38.34 ^s	-29°00'38.38''	2.61	SiO 7-6	16.6 ± 1.8	-5.85	12.6	0.67 ± 0.09	
				SO 8(7)-7(6)	21.6 ± 1.6	-6.27	14.4		
K2	17 ^h 45 ^m 38.23 ^s	-29°00'40.30''	3.03	SiO 7-6	17.5 ± 2.1	-9.06	10.3	0.71 ± 0.1	
				SO 8(7)-7(6)	21.4 ± 1.8	-7.60	11.9		
K3	17 ^h 45 ^m 38.26 ^s	-29°00'41.39''	1.83	SiO 7-6	11.4 ± 1.8	4.86	14.9	0.55 ± 0.1	
				SO 8(7)-7(6)	18.7 ± 1.7	2.45	16.5		
K4	17 ^h 45 ^m 38.40 ^s	-29°00'42.32''	3.35	SiO 7-6	14.6 ± 1.2	-17.53	13.9	0.65 ± 0.06	
				SO 8(7)-7(6)	22.7 ± 1.2	-18.35	13.7		
K5a	17 ^h 45 ^m 38.23 ^s	-29°00'42.06''	3.35	SiO 7-6	9.71 ± 1.5	-15.30	11.7	0.41 ± 0.07	
				SO 8(7)-7(6)	13.7 ± 0.89	-10.31	20.0		
K5b	17 ^h 45 ^m 38.31 ^s	-29°00'42.90''	2.94	SiO 7-6	8.55 ± 1.3	-20.32	14.8	0.59 ± 0.11	
				SO 8(7)-7(6)	16.3 ± 1.5	-20.30	13.1		
K5c	17 ^h 45 ^m 38.22 ^s	-29°00'42.80''	2.11	SiO 7-6	8.55 ± 1.3	-20.32	14.8	0.59 ± 0.11	
				SO 8(7)-7(6)	16.3 ± 1.5	-20.30	13.1		
K6a	17 ^h 45 ^m 38.09 ^s	-29°00'42.12''	3.63	SiO 7-6	11.6 ± 1.1	-1.67	20.7	0.62 ± 0.07	
				SO 8(7)-7(6)	19.4 ± 1.1	-3.04	20.1		
K6b	17 ^h 45 ^m 38.01 ^s	-29°00'42.17''	2.44	SiO 7-6	10.3 ± 1.6	-13.41	19.8	0.58 ± 0.1	
				SO 8(7)-7(6)	19.0 ± 1.7	-12.71	18.6		
K7a	17 ^h 45 ^m 38.12 ^s	-29°00'44.66''	7.20	SiO 7-6	21.4 ± 1.1	-42.07	13.7	0.61 ± 0.04	
				SO 8(7)-7(6)	35.5 ± 1.1	-41.93	13.5		
				CH ₃ OH 2(1,1)-2(0,2)	4.99 ± 0.94	-39.19	15.4		
K7b	17 ^h 45 ^m 38.09 ^s	-29°00'45.52''	2.50	SiO 7-6	12.3 ± 3.0	-50.34	15.3	0.7 ± 0.21	
				SO 8(7)-7(6)	18.3 ± 3.2	-45.76	14.7		
K8a	17 ^h 45 ^m 37.98 ^s	-29°00'47.01''	5.00	SiO 7-6	25.6 ± 1.5	-43.72	25.9	0.69 ± 0.05	
				SO 8(7)-7(6)	41.9 ± 1.7	-44.99	23.0		
K8b	17 ^h 45 ^m 38.02 ^s	-29°00'47.97''	6.10	SiO 7-6	23.9 ± 1.7	-40.48	21.9	1.90 ± 0.33	
					13.1 ± 2.1	-10.80	17.8		0.61 ± 0.11
				SO 8(7)-7(6)	13.1 ± 2.1	-41.07	21.0		
K9	17 ^h 45 ^m 38.41 ^s	-29°00'45.39''	1.83	SiO 7-6	12.4 ± 1.6	-3.19	26.6	0.55 ± 0.08	
					23.7 ± 2.3	-9.99	16.2		
				SO 8(7)-7(6)	24.6 ± 1.7	-5.23	24.4		

Source	α (J2000)	δ (J2000)	Extent (beam)	Emission Line	Flux density (mJy/beam)	v (km s ⁻¹)	Δv (km s ⁻¹)	$I_{\text{SiO}}/I_{\text{SO}}$
K10	17 ^h 45 ^m 38.48 ^s	-29°00'46.14''	2.94	SiO 7-6	13.0 ± 1.6	-24.71	21.0	0.8 ± 0.13
				SO 8(7)-7(6)	18.5 ± 1.8	-23.93	18.4	
K11	17 ^h 45 ^m 38.51 ^s	-29°00'47.07''	1.13	SiO 7-6	11.8 ± 3.7	-16.19	22.7	0.59 ± 0.22
				SO 8(7)-7(6)	23.8 ± 4.4	-20.11	19.0	
K12	17 ^h 45 ^m 38.56 ^s	-29°00'47.52''	1.58	SiO 7-6	13.5 ± 5.2	-28.22	15.4	0.48 ± 0.2
				SO 8(7)-7(6)	29.1 ± 5.3	-28.69	15.0	
K13a	17 ^h 45 ^m 38.60 ^s	-29°00'48.68''	5.85	SiO 7-6	16.3 ± 2.7	-92.39	14.5	0.50 ± 0.18
				SO 8(7)-7(6)	32.37 ± 2.5	-95.18	14.3	
				OCS 25-24	11.1 ± 5.5	-92.99	7.15	
K13b	17 ^h 45 ^m 38.58 ^s	-29°00'49.50''	2.09	SiO 7-6	18.0 ± 7.4	-83.93	16.4	0.51 ± 0.23
				SO 8(7)-7(6)	41.4 ± 8.6	-83.68	14.0	
K14	17 ^h 45 ^m 38.42 ^s	-29°00'46.46''	1.81	SiO 7-6	13.9 ± 3.8	-26.31	14.1	0.73 ± 0.25
				SO 8(7)-7(6)	17.5 ± 3.5	-23.83	15.3	
K15a	17 ^h 45 ^m 38.29 ^s	-29°00'46.18''	4.50	SiO 7-6	19.5 ± 2.3	-9.54	9.75	1.01 ± 0.17
				SO 8(7)-7(6)	17.7 ± 2.1	-8.82	10.6	
K15b	17 ^h 45 ^m 38.30 ^s	-29°00'47.27''	2.85	SiO 7-6	15.7 ± 3.3	2.05	13.7	0.71 ± 0.18
				SO 8(7)-7(6)	22.7 ± 3.4	1.17	13.3	
K16	17 ^h 45 ^m 38.26 ^s	-29°00'49.87''	4.15	SiO 7-6	18.3 ± 5.4	-36.22	10.5	0.5 ± 0.17
				SO 8(7)-7(6)	31.5 ± 4.7	-35.98	12.2	
K17	17 ^h 45 ^m 37.95 ^s	-29°00'50.36''	2.94	SiO 7-6	29.2 ± 8.3	-36.32	16.2	1.05 ± 0.43
				SO 8(7)-7(6)	26.9 ± 8.0	-37.58	16.8	
K18	17 ^h 45 ^m 38.81 ^s	-29°00'40.52''	7.51	SiO 7-6	6.05 ± 1.1	-14.92	14.7	0.6 ± 0.13
				SO 8(7)-7(6)	9.54 ± 1.0	-16.35	15.6	
K19	17 ^h 45 ^m 38.70 ^s	-29°00'38.51''	4.37	SiO 7-6	7.46 ± 0.73	-29.25	29.4	0.91 ± 0.12
				SO 8(7)-7(6)	8.54 ± 0.76	-27.55	28.2	
K20	17 ^h 45 ^m 38.58 ^s	-29°00'31.29''	9.93	SiO 7-6	10.3 ± 1.3	-2.82	19.7	0.53 ± 0.08
				SO 8(7)-7(6)	16.0 ± 1.1	-5.92	24.0	
K21a	17 ^h 45 ^m 38.15 ^s	-29°00'32.82''	2.03	SiO 7-6	17.5 ± 2.3	32.31	27.1	0.74 ± 0.12
				SO 8(7)-7(6)	25.1 ± 2.4	31.28	25.4	
K21b	17 ^h 45 ^m 38.13 ^s	-29°00'32.09''	2.33	SiO 7-6	18.4 ± 4.2	22.53	13.1	0.69 ± 0.19
				SO 8(7)-7(6)	28.6 ± 4.4	21.08	12.3	
K22	17 ^h 45 ^m 37.85 ^s	-29°00'31.02''	3.83	SiO 7-6	13.4 ± 5.7	-8.65	14.5	0.66 ± 0.34
				SO 8(7)-7(6)	18.7 ± 5.3	-9.83	15.7	
K23	17 ^h 45 ^m 37.99 ^s	-29°00'35.57''	5.45	SiO 7-6	6.86 ± 1.8	51.19	10.4	0.47 ± 0.14
				SO 8(7)-7(6)	15.0 ± 1.8	51.66	10.1	
K24	17 ^h 45 ^m 37.97 ^s	-29°00'36.19''	2.49	SiO 7-6	9.11 ± 2.2	-17.10	15.2	0.79 ± 0.24
				SO 8(7)-7(6)	12.6 ± 2.4	-16.90	13.9	
L1	17 ^h 45 ^m 39.60 ^s	-29°01'04.29''	3.67	SiO 7-6	16.1 ± 1.1	-58.68	20.8	0.81 ± 0.07
				SO 8(7)-7(6)	29.1 ± 1.6	-58.91	14.2	
L2	17 ^h 45 ^m 39.74 ^s	-29°01'05.41''	2.25	SiO 7-6	17.2 ± 2.0	-35.33	16.8	0.58 ± 0.08
				SO 8(7)-7(6)	31.7 ± 2.2	-35.60	15.8	

Source	α (J2000)	δ (J2000)	Extent (beam)	Emission Line	Flux density (mJy/beam)	v (km s ⁻¹)	Δv (km s ⁻¹)	$I_{\text{SiO}}/I_{\text{SO}}$
L3	17 ^h 45 ^m 39.79 ^s	-29°01'5.57''	1.02	SiO 7-6	7.95 ± 3.3	-62.66	15.6	0.37 ± 0.16
				SO 8(7)-7(6)	22.4 ± 3.4	-61.95	15.1	
L4	17 ^h 45 ^m 38.80 ^s	-29°01'06.84''	2.18	SiO 7-6	10.3 ± 1.2	-48.40	23.1	0.47 ± 0.06
				SO 8(7)-7(6)	28.2 ± 1.6	-51.13	18.0	
L5	17 ^h 45 ^m 39.66 ^s	-29°01'06.15''	1.99	SiO 7-6	16.7 ± 2.1	-49.29	17.2	0.53 ± 0.08
				SO 8(7)-7(6)	22.4 ± 1.5	-51.23	24.0	
L6	17 ^h 45 ^m 39.70 ^s	-29°01'07.10''	5.11	SiO 7-6	13.0 ± 0.71	-55.02	24.5	0.6 ± 0.04
				SO 8(7)-7(6)	26.6 ± 0.87	-54.88	20.0	
L7	17 ^h 45 ^m 39.75 ^s	-29°01'07.79''	3.20	SiO 7-6	18.9 ± 1.7	-61.44	17.9	0.43 ± 0.04
				SO 8(7)-7(6)	51.2 ± 1.9	-62.67	15.5	
L8	17 ^h 45 ^m 39.68 ^s	-29°01'07.93''	6.58	SiO 7-6	10.1 ± 0.99	-63.48	17.4	0.4 ± 0.04
				SO 8(7)-7(6)	34.2 ± 1.3	-64.93	13.0	
L9	17 ^h 45 ^m 39.81 ^s	-29°01'7.82''	2.25	SiO 7-6	6.18 ± 1.6	-57.91	17.5	0.25 ± 0.07
				SO 8(7)-7(6)	28.4 ± 1.8	-60.78	15.3	
L10a	17 ^h 45 ^m 39.81 ^s	-29°01'8.68''	2.20	SiO 7-6	12.1 ± 2.4	-60.44	15.2	0.34 ± 0.07
				SO 8(7)-7(6)	28.9 ± 1.9	-59.95	18.6	
L10b	17 ^h 45 ^m 39.78 ^s	-29°01'08.75''	2.80	SiO 7-6	14.6 ± 1.6	-64.80	21.1	0.46 ± 0.06
				SO 8(7)-7(6)	39.1 ± 2.0	-64.58	17.2	
L11	17 ^h 45 ^m 30.80 ^s	-29°01'09.66''	3.50	SiO 7-6	8.47 ± 3.8	-64.30	7.15	0.2 ± 0.09
				SO 8(7)-7(6)	17.3 ± 1.5	-69.77	17.7	
L12	17 ^h 45 ^m 39.88 ^s	-29°01'9.93''	1.78	SiO 7-6	7.32 ± 2.3	-34.75	19.8	0.59 ± 0.22
				SO 8(7)-7(6)	15.0 ± 2.8	-35.23	16.3	
L13	17 ^h 45 ^m 39.88 ^s	-29°01'4.67''	5.74	SiO 7-6	7.62 ± 0.31	-46.78	36.6	0.51 ± 0.02
				SO 8(7)-7(6)	18.1 ± 0.38	-46.09	30.0	
L14	17 ^h 45 ^m 39.91 ^s	-29°01'4.06''	4.39	SiO 7-6	10.1 ± 0.59	-58.36	24.2	0.62 ± 0.04
				SO 8(7)-7(6)	15.5 ± 0.55	-55.07	25.6	
L15	17 ^h 45 ^m 39.96 ^s	-29°01'3.62''	1.78	SiO 7-6	18.2 ± 2.3	-59.76	14.5	0.48 ± 0.07
				SO 8(7)-7(6)	30.8 ± 1.9	-58.14	17.7	
L16	17 ^h 45 ^m 40.00 ^s	-29°01'3.38''	1.70	SiO 7-6	10.3 ± 1.4	-52.46	22.9	0.5 ± 0.08
				SO 8(7)-7(6)	26.9 ± 1.8	-51.29	17.5	
L17	17 ^h 45 ^m 40.05 ^s	-29°01'2.33''	4.53	SiO 7-6	30.9 ± 0.99	-65.43	18.2	0.74 ± 0.03
				SO 8(7)-7(6)	35.1 ± 0.83	-64.85	21.6	
L18	17 ^h 45 ^m 40.09 ^s	-29°01'2.60''	2.97	SiO 7-6	14.1 ± 0.86	-49.59	23.6	0.59 ± 0.04
				SO 8(7)-7(6)	25.9 ± 0.92	-49.22	21.9	
L19	17 ^h 45 ^m 40.12 ^s	-29°01'1.78''	4.07	SiO 7-6	9.37 ± 1.3	-45.00	13.8	0.47 ± 0.07
					28.3 ± 0.92	-69.00	20.2	0.80 ± 0.03
				SO 8(7)-7(6)	18.0 ± 1.2	-46.16	15.2	
					35.8 ± 0.92	-68.97	20.0	

Source	α (J2000)	δ (J2000)	Extent (beam)	Emission Line	Flux density (mJy/beam)	v (km s ⁻¹)	Δv (km s ⁻¹)	$I_{\text{SiO}}/I_{\text{SO}}$
L20	17 ^h 45 ^m 40.14 ^s	-29°01'1.13''	2.73	SiO 7-6	24.5 ± 1.3	-48.49	20.2	0.65 ± 0.04
				SO 8(7)-7(6)	48.4 ± 1.7	-48.64	15.8	
L21	17 ^h 45 ^m 40.15 ^s	-29°01'00.44''	3.22	SiO 7-6	16.9 ± 1.2	-51.05	17.8	0.47 ± 0.04
				SO 8(7)-7(6)	31.4 ± 1.1	-52.57	20.4	
L22	17 ^h 45 ^m 40.181 ^s	-29°01'00.89''	2.52	SiO 7-6	26.4 ± 1.4	-47.16	19.5	0.54 ± 0.03
				SO 8(7)-7(6)	44.5 ± 1.3	-47.60	21.3	
L23	17 ^h 45 ^m 40.19 ^s	-29°01'1.47''	2.88	SiO 7-6	15.2 ± 0.94	-48.15	29.4	0.52 ± 0.04
				SO 8(7)-7(6)	32.6 ± 1.1	-48.62	26.2	
L24	17 ^h 45 ^m 40.25 ^s	-29°01'00.94''	4.02	SiO 7-6	17.1 ± 1.1	-62.84	22.1	0.46 ± 0.03
				SO 8(7)-7(6)	37.1 ± 1.1	-62.44	22.0	
L25	17 ^h 45 ^m 40.20 ^s	-29°01'00.14''	2.94	SiO 7-6	17.5 ± 0.92	-61.57	29.6	0.66 ± 0.04
				SO 8(7)-7(6)	28.7 ± 1.0	-58.58	27.2	
L26	17 ^h 45 ^m 40.27 ^s	-29°00'59.59''	3.35	SiO 7-6	12.4 ± 1.2	-52.84	22.7	0.53 ± 0.06
				SO 8(7)-7(6)	22.6 ± 1.2	-51.51	23.3	
L27	17 ^h 45 ^m 40.28 ^s	-29°00'58.81''	1.69	SiO 7-6	17.7 ± 2.8	-30.47	18.8	0.56 ± 0.1
				SO 8(7)-7(6)	26.5 ± 2.3	-29.15	22.6	
L28	17 ^h 45 ^m 40.46 ^s	-29°00'59.67''	89.40	SiO 7-6	12.7 ± 0.84	-60.86	19.5	0.62 ± 0.05
				SO 8(7)-7(6)	18.7 ± 0.77	-59.57	21.2	
L29	17 ^h 45 ^m 40.19 ^s	-29°01'3.83''	3.09	SiO 7-6	7.54 ± 0.99	-49.50	21.6	0.55 ± 0.08
				SO 8(7)-7(6)	12.2 ± 0.88	-53.33	24.2	
L30	17 ^h 45 ^m 40.47 ^s	-29°01'8.10''	3.52	SiO 7-6	14.0 ± 3.1	-26.48	14.9	0.89 ± 0.21
					6.18 ± 4.2	-52.43	10.9	13.46 ± 9.69
				SO 8(7)-7(6)	21.6 ± 2.0	-30.01	10.9	
					12.7 ± 2.7	-63.94	0.394	
M1	17 ^h 45 ^m 41.31 ^s	-29°00'58.84''	4.50	SiO 7-6	8.67 ± 1.0	-45.25	14.4	0.65 ± 0.09
				SO 8(7)-7(6)	13.8 ± 1.1	-44.42	14.0	
M2	17 ^h 45 ^m 41.41 ^s	-29°00'59.93''	1.00	SiO 7-6	2.98 ± 0.63	-50.17	18.2	0.38 ± 0.09
				SO 8(7)-7(6)	8.22 ± 0.66	-54.28	17.2	
M3	17 ^h 45 ^m 41.38 ^s	-29°00'58.16''	2.02	SiO 7-6	6.39 ± 1.9	-42.64	15.4	0.43 ± 0.14
				SO 8(7)-7(6)	9.23 ± 1.2	-44.63	24.8	
M4	17 ^h 45 ^m 41.23 ^s	-29°00'57.77''	2.27	SO 8(7)-7(6)	10.8 ± 3.2	23.10	8.21	
				CH ₃ OH 2(1,1)-2(0,2)	8.19 ± 2.2	21.39	12.0	

C. INFERRED CONDITIONS

Table 4. The points of highest posterior density (HPD) of the physical conditions towards each observational source. Sources with parameter entries marked with – represent an unconstrained value in that dimension.

Source	T_{kin} [K]	$\log n_{\text{H}}$ [cm^{-3}]	$\log N_{\text{SiO}}$ [cm^{-2}]	$\log N_{\text{SO}}$ [cm^{-2}]
N8	–	–	$13.30^{+0.85}_{-0.68}$	$14.65^{+0.56}_{-0.23}$
N7a	–	$6.73^{+0.26}_{-1.70}$	$12.92^{+0.61}_{-0.13}$	$14.202^{+0.421}_{-0.071}$
N7b	–	$5.70^{+0.80}_{-0.72}$	$12.830^{+0.378}_{-0.073}$	$14.027^{+0.258}_{-0.049}$
C1	440^{+300}_{-240}	$5.74^{+0.62}_{-0.31}$	$13.416^{+0.142}_{-0.053}$	$14.593^{+0.144}_{-0.051}$
G1	310^{+490}_{-110}	$5.69^{+0.65}_{-0.51}$	$13.45^{+0.22}_{-0.12}$	$14.489^{+0.161}_{-0.100}$
G2	610^{+140}_{-180}	$5.88^{+0.16}_{-0.18}$	$13.392^{+0.058}_{-0.064}$	$14.500^{+0.075}_{-0.058}$
G3a	81^{+159}_{-18}	6.56 ± 0.29	$13.648^{+0.106}_{-0.095}$	$14.717^{+0.115}_{-0.080}$
G3b	108^{+182}_{-45}	$6.42^{+0.45}_{-0.27}$	$13.710^{+0.114}_{-0.087}$	$14.905^{+0.126}_{-0.062}$
G4	–	$6.21^{+0.56}_{-0.31}$	$13.50^{+0.20}_{-0.13}$	$14.639^{+0.199}_{-0.081}$
G5	63^{+22}_{-0}	$6.99^{+0.00}_{-0.31}$	13.981 ± 0.090	$14.985^{+0.055}_{-0.058}$
D1	–	–	$13.59^{+0.40}_{-0.12}$	$14.725^{+0.275}_{-0.069}$
D2	300^{+450}_{-100}	$5.76^{+0.49}_{-0.44}$	$13.53^{+0.19}_{-0.11}$	$14.704^{+0.115}_{-0.090}$
D3c1	–	$5.99^{+0.61}_{-0.75}$	$13.13^{+0.31}_{-0.13}$	$14.37^{+0.22}_{-0.10}$
D3c2	520^{+320}_{-310}	$5.81^{+0.57}_{-0.60}$	$13.11^{+0.24}_{-0.14}$	$14.417^{+0.178}_{-0.096}$
D4	297^{+509}_{-98}	$5.72^{+0.56}_{-0.52}$	$13.408^{+0.199}_{-0.083}$	$14.594^{+0.131}_{-0.057}$
D5	340^{+410}_{-210}	$5.78^{+0.67}_{-0.63}$	$13.10^{+0.31}_{-0.15}$	$14.55^{+0.19}_{-0.10}$
D6	–	$5.83^{+1.16}_{-0.76}$	$13.33^{+0.56}_{-0.20}$	$14.45^{+0.39}_{-0.16}$
D7	–	$6.40^{+0.59}_{-1.26}$	$13.32^{+0.55}_{-0.21}$	$14.47^{+0.37}_{-0.12}$
H1a	–	$5.74^{+0.69}_{-0.50}$	$13.558^{+0.225}_{-0.076}$	$14.635^{+0.152}_{-0.089}$
H1b	–	$5.90^{+0.65}_{-0.51}$	$13.809^{+0.180}_{-0.069}$	$14.713^{+0.154}_{-0.094}$
H2	–	$5.95^{+0.90}_{-1.34}$	$13.57^{+0.74}_{-0.13}$	$14.31^{+0.49}_{-0.20}$
H3	–	$6.84^{+0.15}_{-1.83}$	$13.75^{+0.62}_{-0.13}$	$14.52^{+0.43}_{-0.23}$
H4	–	$6.63^{+0.36}_{-1.48}$	$13.774^{+0.556}_{-0.095}$	$14.47^{+0.37}_{-0.12}$
J1	–	$5.67^{+1.05}_{-0.27}$	$13.36^{+0.30}_{-0.17}$	$14.38^{+0.21}_{-0.16}$
J2	–	–	$14.239^{+0.316}_{-0.052}$	$14.859^{+0.276}_{-0.051}$
J3	–	$5.69^{+0.85}_{-0.14}$	$13.448^{+0.187}_{-0.088}$	$14.593^{+0.175}_{-0.046}$
J4	–	–	$13.29^{+0.45}_{-0.22}$	$14.33^{+0.29}_{-0.18}$
K1	480^{+380}_{-240}	$5.93^{+0.68}_{-0.56}$	$13.46^{+0.23}_{-0.12}$	$14.61^{+0.19}_{-0.10}$
K2	450^{+370}_{-260}	–	$13.39^{+0.42}_{-0.13}$	$14.532^{+0.280}_{-0.099}$
K3	–	$5.67^{+1.32}_{-0.43}$	$13.37^{+0.48}_{-0.16}$	$14.614^{+0.321}_{-0.095}$
K4	460^{+290}_{-310}	$5.84^{+0.46}_{-0.68}$	$13.45^{+0.24}_{-0.11}$	$14.63^{+0.15}_{-0.10}$
K5a	–	$5.61^{+1.16}_{-0.29}$	$13.20^{+0.34}_{-0.16}$	$14.57^{+0.25}_{-0.11}$
K5b	–	$5.87^{+1.12}_{-0.56}$	$13.24^{+0.41}_{-0.15}$	$14.446^{+0.303}_{-0.081}$
K5c	–	$5.87^{+0.85}_{-0.60}$	$13.25^{+0.34}_{-0.17}$	$14.47^{+0.24}_{-0.12}$
K6a	360^{+400}_{-200}	$5.73^{+0.76}_{-0.47}$	$13.51^{+0.27}_{-0.12}$	$14.72^{+0.18}_{-0.10}$
K6b	–	$5.82^{+0.99}_{-0.79}$	$13.46^{+0.47}_{-0.14}$	$14.668^{+0.294}_{-0.089}$
K7a	–	$5.65^{+0.85}_{-0.32}$	$13.594^{+0.188}_{-0.072}$	$14.784^{+0.151}_{-0.042}$
K7b	–	5.9 ± 1.0	$13.44^{+0.61}_{-0.24}$	$14.58^{+0.44}_{-0.20}$
K8a	590^{+210}_{-340}	$5.78^{+0.46}_{-0.45}$	$13.97^{+0.17}_{-0.11}$	$15.108^{+0.127}_{-0.097}$
K8bc1	–	$6.20^{+0.79}_{-1.20}$	$13.848^{+0.595}_{-0.097}$	$14.58^{+0.39}_{-0.15}$
K8bc2	–	$5.84^{+1.15}_{-0.46}$	$13.52^{+0.34}_{-0.16}$	$14.703^{+0.254}_{-0.086}$

Source	T_{kin} [K]	$\log n_{\text{H}}$ [cm^{-3}]	$\log N_{\text{SiO}}$ [cm^{-2}]	$\log N_{\text{SO}}$ [cm^{-2}]
K9	–	$6.09^{+0.53}_{-0.77}$	$13.65^{+0.30}_{-0.12}$	$14.907^{+0.215}_{-0.097}$
K10	–	$5.93^{+1.06}_{-0.63}$	$13.58^{+0.44}_{-0.13}$	$14.654^{+0.301}_{-0.088}$
K11	–	$5.77^{+1.22}_{-0.77}$	$13.61^{+0.62}_{-0.32}$	$14.83^{+0.38}_{-0.20}$
K12	–	–	$13.49^{+0.73}_{-0.47}$	$14.81^{+0.42}_{-0.21}$
K13a	–	$6.01^{+0.82}_{-0.86}$	$13.53^{+0.36}_{-0.18}$	$14.787^{+0.263}_{-0.072}$
K13b	–	–	$13.68^{+0.73}_{-0.51}$	$14.95^{+0.43}_{-0.22}$
K14	580^{+360}_{-290}	–	$13.48^{+0.68}_{-0.31}$	$14.59^{+0.50}_{-0.24}$
K15a	470^{+400}_{-240}	$5.85^{+1.14}_{-0.65}$	$13.43^{+0.44}_{-0.14}$	$14.41^{+0.31}_{-0.14}$
K15b	720^{+280}_{-360}	$6.16^{+0.83}_{-1.05}$	$13.50^{+0.51}_{-0.21}$	$14.63^{+0.35}_{-0.15}$
K16	–	$5.66^{+1.33}_{-0.60}$	$13.47^{+0.57}_{-0.30}$	$14.73^{+0.36}_{-0.14}$
K17	–	–	$13.87^{+0.79}_{-0.31}$	$14.84^{+0.63}_{-0.35}$
K18	–	$6.32^{+0.68}_{-1.11}$	$13.11^{+0.48}_{-0.19}$	$14.30^{+0.33}_{-0.10}$
K19	–	$5.81^{+1.17}_{-0.55}$	$13.47^{+0.41}_{-0.11}$	$14.494^{+0.286}_{-0.084}$
K20	–	$5.43^{+0.98}_{-0.45}$	$13.46^{+0.37}_{-0.14}$	$14.71^{+0.23}_{-0.12}$
K21a	–	$5.82^{+1.17}_{-0.47}$	$13.82^{+0.38}_{-0.13}$	$14.931^{+0.263}_{-0.086}$
K21b	610^{+270}_{-380}	$6.04^{+0.92}_{-1.08}$	$13.54^{+0.59}_{-0.22}$	$14.70^{+0.39}_{-0.17}$
K22	–	–	$13.50^{+0.86}_{-0.58}$	$14.65^{+0.63}_{-0.33}$
K23	–	$5.88^{+1.07}_{-0.66}$	$13.01^{+0.51}_{-0.25}$	$14.31^{+0.35}_{-0.13}$
K24	917^{+81}_{-574}	$5.74^{+1.25}_{-0.93}$	$13.31^{+0.75}_{-0.25}$	$14.40^{+0.53}_{-0.24}$
L1	610^{+190}_{-420}	$5.65^{+0.67}_{-0.45}$	$13.66^{+0.25}_{-0.11}$	$14.739^{+0.160}_{-0.096}$
L2	–	$5.75^{+0.63}_{-0.52}$	$13.61^{+0.25}_{-0.14}$	$14.84^{+0.16}_{-0.12}$
L3	480^{+360}_{-320}	$5.85^{+1.00}_{-0.91}$	$13.29^{+0.67}_{-0.52}$	$14.68^{+0.41}_{-0.17}$
L4	580^{+230}_{-410}	$5.68^{+0.80}_{-0.47}$	$13.52^{+0.26}_{-0.13}$	$14.828^{+0.189}_{-0.095}$
L5	–	–	$13.60^{+0.37}_{-0.12}$	$14.843^{+0.271}_{-0.063}$
L6	560^{+220}_{-330}	$5.77^{+0.58}_{-0.31}$	$13.631^{+0.156}_{-0.093}$	$14.85^{+0.13}_{-0.10}$
L7	–	$5.69^{+0.63}_{-0.53}$	$13.68^{+0.24}_{-0.13}$	$15.029^{+0.160}_{-0.095}$
L8	–	$5.76^{+0.66}_{-0.42}$	$13.38^{+0.20}_{-0.12}$	$14.78^{+0.15}_{-0.11}$
L9	–	$5.63^{+1.08}_{-0.42}$	$13.20^{+0.38}_{-0.24}$	$14.78^{+0.25}_{-0.12}$
L10a	580^{+310}_{-340}	$5.46^{+1.07}_{-0.41}$	$13.41^{+0.35}_{-0.18}$	$14.86^{+0.24}_{-0.10}$
L10b	–	$5.78^{+0.58}_{-0.59}$	$13.64^{+0.25}_{-0.13}$	$14.96^{+0.16}_{-0.10}$
L11	–	–	$12.97^{+0.54}_{-0.51}$	$14.604^{+0.324}_{-0.076}$
L12	–	$6.20^{+0.79}_{-1.26}$	$13.35^{+0.64}_{-0.35}$	$14.55^{+0.44}_{-0.21}$
L13	510^{+260}_{-270}	$5.72^{+0.50}_{-0.37}$	$13.58^{+0.17}_{-0.10}$	$14.847^{+0.112}_{-0.085}$
L14	420^{+340}_{-240}	$5.79^{+0.65}_{-0.42}$	$13.513^{+0.200}_{-0.090}$	$14.721^{+0.148}_{-0.095}$
L15	350^{+410}_{-190}	$5.71^{+0.78}_{-0.52}$	$13.56^{+0.27}_{-0.14}$	$14.863^{+0.195}_{-0.096}$
L16	480^{+390}_{-240}	$5.79^{+0.93}_{-0.39}$	$13.51^{+0.28}_{-0.13}$	$14.81^{+0.21}_{-0.11}$
L17	500^{+300}_{-230}	$5.78^{+0.50}_{-0.33}$	$13.876^{+0.135}_{-0.075}$	$14.998^{+0.113}_{-0.083}$
L18	–	$5.83^{+0.52}_{-0.46}$	$13.66^{+0.17}_{-0.10}$	$14.869^{+0.144}_{-0.092}$
L19c1	680^{+320}_{-290}	$5.81^{+0.62}_{-0.77}$	$13.26^{+0.31}_{-0.16}$	$14.559^{+0.230}_{-0.097}$
L19c2	–	$5.88^{+0.47}_{-0.41}$	$13.886^{+0.146}_{-0.082}$	$14.979^{+0.118}_{-0.088}$
L20	500^{+290}_{-260}	$5.88^{+0.46}_{-0.44}$	$13.828^{+0.147}_{-0.094}$	$15.002^{+0.137}_{-0.083}$
L21	560^{+190}_{-410}	$5.80^{+0.55}_{-0.53}$	$13.61^{+0.21}_{-0.10}$	$14.928^{+0.145}_{-0.086}$
L22	–	$5.75^{+0.62}_{-0.32}$	$13.845^{+0.172}_{-0.093}$	$15.095^{+0.137}_{-0.083}$
L23	–	$5.77^{+0.61}_{-0.38}$	$13.781^{+0.162}_{-0.090}$	$15.052^{+0.134}_{-0.089}$
L24	590^{+140}_{-370}	$5.82^{+0.47}_{-0.43}$	$13.706^{+0.180}_{-0.098}$	$15.040^{+0.119}_{-0.099}$

Source	T_{kin} [K]	$\log n_{\text{H}}$ [cm^{-3}]	$\log N_{\text{SiO}}$ [cm^{-2}]	$\log N_{\text{SO}}$ [cm^{-2}]
L25	300^{+420}_{-130}	$5.74^{+0.45}_{-0.51}$	$13.85^{+0.23}_{-0.11}$	$15.016^{+0.122}_{-0.094}$
L26	580^{+260}_{-350}	$5.86^{+0.67}_{-0.56}$	$13.58^{+0.24}_{-0.11}$	$14.85^{+0.18}_{-0.11}$
L27	360^{+430}_{-210}	$5.82^{+0.68}_{-0.57}$	$13.67^{+0.28}_{-0.17}$	$14.92^{+0.18}_{-0.13}$
L28	350^{+460}_{-150}	$5.89^{+0.55}_{-0.54}$	$13.54^{+0.19}_{-0.11}$	$14.719^{+0.152}_{-0.097}$
L29	–	$5.79^{+0.72}_{-0.55}$	$13.35^{+0.26}_{-0.15}$	$14.59^{+0.20}_{-0.11}$
L30c1	490^{+410}_{-240}	$5.99^{+0.89}_{-0.68}$	$13.48^{+0.43}_{-0.21}$	$14.50^{+0.30}_{-0.11}$
L30c2	450^{+410}_{-270}	–	$13.02^{+0.62}_{-1.01}$	
M1	400^{+460}_{-170}	$5.65^{+0.87}_{-0.58}$	$13.23^{+0.36}_{-0.14}$	$14.42^{+0.23}_{-0.12}$
M2	510^{+370}_{-290}	–	$12.89^{+0.39}_{-0.19}$	$14.27^{+0.28}_{-0.10}$
M3	–	$6.78^{+0.17}_{-1.49}$	$13.17^{+0.51}_{-0.27}$	$14.50^{+0.35}_{-0.13}$